

## SN 2023axu: A Type IIP Supernova Interacted with a Low-Density Stellar Wind

ZEYI WANG,<sup>1,2,3</sup> JUJIA ZHANG <sup>1,2</sup> QIAN ZHAI <sup>1,2</sup> LIPING LI <sup>1,2</sup> G. VALERIN <sup>4</sup> A. REGUITTI <sup>4</sup>  
A. PASTORELLO <sup>4</sup> ZHENYU WANG <sup>1,2,3</sup> ZEYI ZHAO <sup>1,2,3</sup> TENGFEI SONG <sup>1</sup> AND YONGZHI CAI <sup>1,2,4</sup>

<sup>1</sup>*Yunnan Observatories (YNAO), Chinese Academy of Sciences (CAS), Kunming, 650216, China*

<sup>2</sup>*International Centre of Supernovae (ICESUN), Yunnan Key Laboratory of Supernova Research, Kunming 650216*

<sup>3</sup>*School of Astronomy and Space Science, University of Chinese Academy of Sciences, Beijing, 101408, China*

<sup>4</sup>*Osservatorio Astronomico di Padova, Vicolo dell'Osservatorio 5, 35122 Padova, Italy*

### ABSTRACT

We present photometric and spectroscopic observations of Type IIP supernova SN 2023axu, spanning  $\sim 400$  d after the explosion. Its light curve is typical of normal SNe IIP, with a  $V$ -band peak of  $17.25 \pm 0.06$  mag and no early-time excess indicative of strong circumstellar interaction. The early spectra exhibit a distinctive broad “ledge” near 4600 Å. Through spectral modeling and comparison, we attribute this feature to a blend of C, N, and He lines excited by weak interaction between the ejecta and a low-density stellar wind. The late-time photometric evolution shows no discernible contribution from interaction, arguing against strong late-time circumstellar material engagement and supporting the low density wind scenario. From modeling, this SN synthesized  $\sim 0.055 M_{\odot}$  of  $^{56}\text{Ni}$ , and nebular spectrum analysis indicates a progenitor mass near  $15 M_{\odot}$ . SN 2023axu thus exemplifies weak ejecta–wind interaction and highlights the diversity of mass-loss histories and circumstellar environments of SNe II progenitor.

*Keywords:* supernovae: general — supernovae: individual (SN 2023axu), core-collapse supernova, Stellar mass loss

### 1. INTRODUCTION

Core-collapse supernovae (CCSNe; A. Heger et al. 2003) mark the explosive endpoints of massive stars ( $M > 8 M_{\odot}$ ), serving as vital probes of their final evolutionary stages, including mass-loss history and circumstellar environments. As the most numerous class of CCSNe, Type II SNe (SNe II) retain a substantial hydrogen envelope at the time of explosion. The interaction between the expanding ejecta and pre-existing circumstellar material (CSM) is a critical process in SNe II. It can be a dominant source of emission, particularly at early phases and serves as a unique diagnostic for the mass-loss history of the progenitor star (N. Smith 2014).

Observations reveal a broad continuum of CSM interaction strengths. For instance, SNe IIn exhibit long-lived narrow emission lines along with luminous, slowly declining light curves, indicating sustained interaction with dense, confined CSM (e.g., T. Zhang et al. 2012; A. Gal-Yam et al. 2014; L. Tartaglia et al. 2020). In contrast, normal SNe IIP—characterized by an opti-

cal plateau powered by hydrogen recombination (D. V. Popov 1993)—typically show little evidence of ongoing CSM interaction. SNe IIL, which are defined by their light curves that decline almost linearly in magnitude, also fall into this category of generally weak interaction. However, a growing sample of early-time spectra has identified relatively short-lived flash-ionized features in some SNe IIP/IIL, implying the presence of confined CSM that is quickly overrun by the ejecta (e.g., O. Yaron et al. 2017; J. Zhang et al. 2020; R. J. Bruch et al. 2021, 2023; W. V. Jacobson-Galán et al. 2024).

High-cadence studies of nearby SNe II have recently revolutionized our view of this brief interaction phase. Landmark events such as SN 2023ixf and SN 2024ggi, for instance, have enabled the detailed capture of early shock breakout signals and the direct probing of dense CSM shed in the progenitor’s final years (e.g., K. A. Bostroem et al. 2023a; N. Smith et al. 2023; G. Li et al. 2024; E. A. Zimmerman et al. 2024; J. Zhang et al. 2024; Y. Yang et al. 2025). These studies indicate that mass-loss rates can increase by orders of magnitude shortly before explosion, unveiling vigorous pre-SN activity in

red supergiant progenitors (e.g., J. Zhang et al. 2023; M. Shrestha et al. 2024; D. Xiang et al. 2024).

Beyond these recognized signatures of clear but often short-lived interaction, there may exist SNe exhibiting even weaker and more fleeting CSM interaction. A potential spectroscopic indicator is a broad emission “ledge” near  $4600 \text{ \AA}$  observed in the early-phase spectra of some SNe II (e.g., T. Szalai et al. 2019; M. T. Soumagnac et al. 2020; H. Lin et al. 2025). The origin of this feature remains debated; proposed explanations include blending of metal lines (e.g., C, N, He) or a signature of weak interaction with a low-density, extended stellar wind (G. Hosseinzadeh et al. 2018; R. J. Bruch et al. 2021). If it indeed stems from weak CSM interaction, this ledge could provide a unique window into low mass-loss regimes that are difficult to detect through traditional narrow-line signatures.

SN 2023axu presents an excellent case to test this scenario. It displays the distinct ledge feature in its early spectra, while its overall light curve evolution closely follows that of normal SNe IIP, showing no signs of the significant early-time excess brightness indicative of strong CSM thermalization. This presents a clear dichotomy: a spectroscopic hint of interaction alongside photometric behavior consistent with a tenuous CSM environment. While the ledge feature has been analyzed by M. Shrestha et al. (2024), our study conducts an independent and comprehensive investigation based on extensive photometric and spectroscopic observations spanning approximately 1000 days. This dataset allows us to measure the key parameters of SN 2023axu, analyze the origin of the controversial ledge feature, and discuss its late-time evolution. Our findings suggests that the properties of SN 2023axu are consistently explained by weak ejecta interaction with a low-density stellar wind, providing an example of a SN II progenitor with modest terminal mass loss. This work highlights the diversity of pre-SN mass-loss histories and underscores the importance of subtle spectroscopic signatures in uncovering them.

The paper is structured as follows: Section 2 describes the observations and data reduction. Section 3 presents the analysis of the light curves, bolometric luminosity, spectral evolution, and nickel mass. Section 4 discusses the physics of the ledge feature, the inferred progenitor and CSM properties, and the implications for our understanding of SNe II diversity. Section 5 provides a summary of our conclusions.

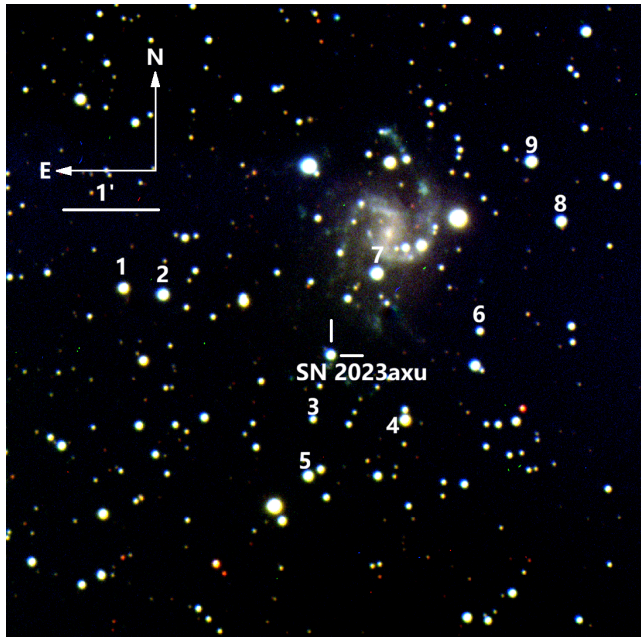


**Figure 1.** Finder chart for SN 2023axu in the galaxy NGC 2283. The local reference stars listed in Table A1 are marked with a nearby number. The image is a color composite created from g-, r-, and i-band observations obtained with the YFOSC instrument on the LJT.

## 2. OBSERVATIONS

### 2.1. Discovery

SN 2023axu was discovered by the Distance Less Than 40 Mpc (DLT40) survey on January 28, 2023 (MJD 59972.11), in a clear-filter image with a magnitude of  $15.64 \pm 0.01$  (D. J. Sand et al. 2023). It is located at J2000 coordinates  $RA = 06^{\text{h}}45^{\text{m}}55^{\text{s}}.32$ ,  $Dec = -18^{\circ}13'53''.52$ , in the SB(s)c spiral galaxy NGC 2283 (Figure 1), at a heliocentric redshift of  $z = 0.002805 \pm 0.000005$  (B. S. Koribalski et al. 2004). K. A. Bostroem et al. (2023b) classified SN 2023axu as a young SN II based on its blue continuum and weak, broad hydrogen features. Ten hours later, an independent SN II classification was reported by L. Li et al. (2023) based on observations with the 2.4 m Li-Jiang Telescope (LJT; Y.-F. Fan et al. 2015) at the Li-Jiang Observatory of Yunnan Observatories. The LJT, equipped with the Yunnan Faint Object Spectrograph and Camera (YFOSC; C.-J. Wang et al. 2019), was subsequently employed for ongoing photometric and spectroscopic monitoring of this SN.

### 2.2. Photometry

Figure 2 presents the optical and near-infrared light curves of SN 2023axu, covering a period of about 410 d, as obtained with LJT, Wumingshan 60cm Telescope (WMS) at Daocheng, the Rapid Eye Mount (REM) and

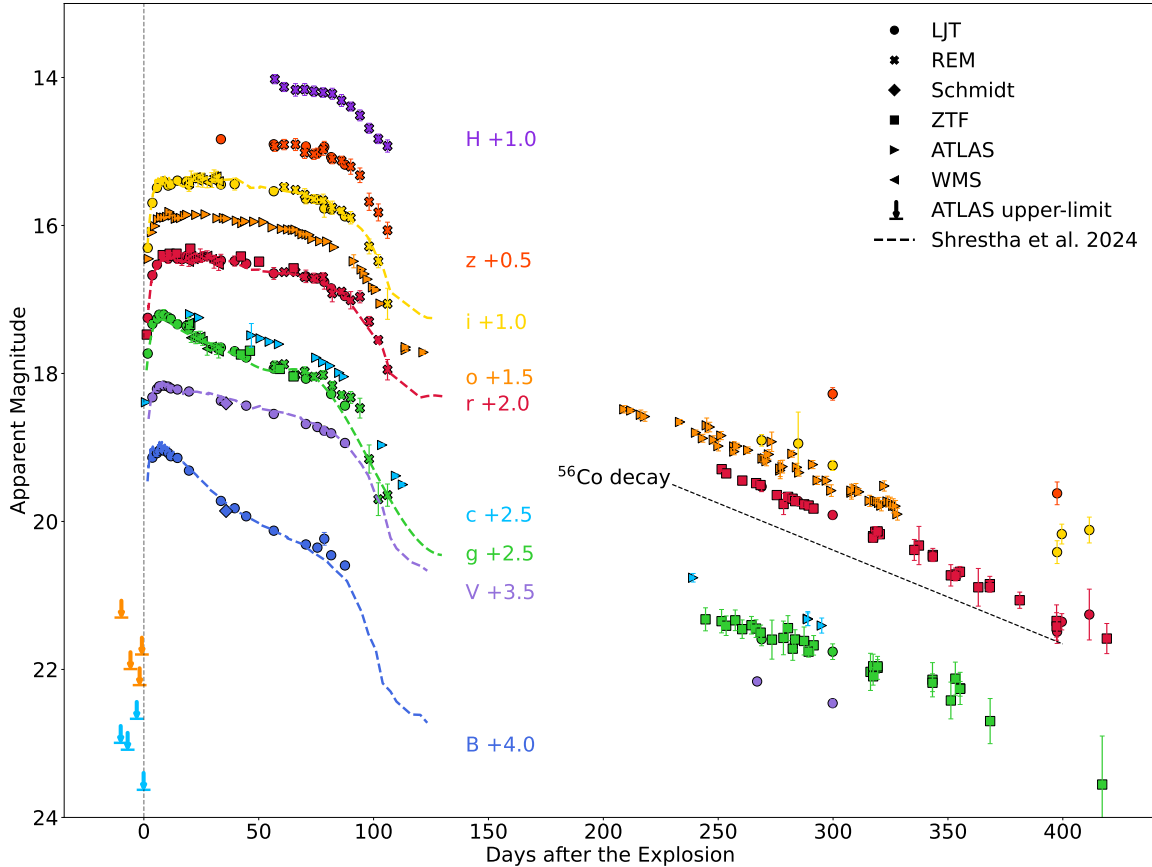


**Figure 2.** Light curves of SN 2023axu. The different bands are vertically shifted for clarity. Data from various telescopes and sources are indicated accordingly.

Schmidt 67/92 telescopes. All images were processed following standard IRAF procedures, which included bias subtraction, flat-fielding, cosmic ray removal, and template subtraction. The point-spread-function (PSF) fitting method (P. B. Stetson 1987) was used to obtain instrumental magnitudes. These instrumental magnitudes were subsequently converted into standard Johnson  $BV$  (H. L. Johnson et al. 1966), standard Sloan  $griz$  (AB magnitude) and 2MASS H-band (Vega magnitude). For reference, data from M. Shrestha et al. (2024) are overlaid, showing a light-curve evolution that matches our observations well. Additionally, we acquired publicly available data from both the ATLAS survey (c-band and o-band) and the ZTF survey (g-band and i-band), which cover the late stages of SN 2023axu.

Based on shock-cooling model fits, M. Shrestha et al. (2024) estimated the explosion date of SN 2023axu to be  $\text{MJD} = 59971.48 \pm 0.03$ . To independently constrain the explosion epoch, we applied a simple expanding fireball model to the early-time r-band light curve, expressed as:  $F(t) = A \times (t - t_0)^2 + B$ . The best fit yields coefficients of  $A = 7.49 \times 10^{-16}$  and  $B = 1.28 \times 10^{-15}$ , resulting in  $t_0 = 59971.5 \pm 0.5$ . Considering the combined statistical

uncertainty from the fireball model fit and the potential systematic offset between the model assumption and the actual explosion epoch, we adopt  $59971.5 \pm 0.5$  as the explosion time of SN 2023axu. This result is consistent with the ATLAS non-detection on  $\text{MJD} = 59970.89$  (c-band upper limit at  $\sim 20.3$  mag) and its first detection on  $\text{MJD} = 59971.91$  (c-band magnitude of  $15.93 \pm 0.01$  mag).

The archival Hubble Space Telescope (HST) observations of SN 2023axu (Program 17502; PI: David Thilker) were obtained using the Wide Field Camera 3 (WFC3/UVIS) on September 24, 2025 (MJD 60942.8), providing late-time photometry approximately 1000 days after the explosion. These data are publicly accessible through the Mikulski Archive for Space Telescopes (MAST) at STScI and are listed in Table A4. We retrieved the Level 3 calibrated images from MAST, reduced with the version 12.1.4 of the HST Calibration Reference Data System (CRDS). We performed PSF photometry on the source identified at the coordinates

of SN 2023axu with the ECSNOOPY pipeline<sup>5</sup> v. 3.1.029, specifically adapted to run on images from space telescopes (see A. Reguitti et al. 2025). A forced PSF photometry is performed at the expected position of the transient. If no source is fitted with a flux higher than the decided threshold, then a limiting magnitude is provided with a flux equal to the selected threshold. Finally, the calibration of the instrumental magnitudes was done by calculating the photometric zero points in the AB scale with the formula<sup>6</sup>:

$$ZP_{AB} = -2.5 \log_{10}(\text{PHOTFLAM}) - 5 \log_{10}(\text{PHOTPLAM}) - 2.408 \quad (1)$$

the PHOTFLAM and PHOTPLAM values were retrieved from the respective keywords stored in the header of the images. In case the source is not identified (as in the *F275W* and *F336W* filters), we estimated a  $3\sigma$  upper limit.

### 2.3. Spectroscopy

A total of 16 spectra of SN 2023axu were obtained with YFOSC on the LJT, covering the period from approximately 1 to 288 d after explosion. Wavelength and flux calibration were performed using standard IRAF procedures. Telluric absorption features were removed by comparison with standard star observations, and atmospheric extinction corrections were applied using local extinction data. To achieve complete phase coverage, the spectral series shown in Figure 3 comprises data from the LJT, supplemented by one spectrum retrieved from the Transient Name Server (obtained by the DLT40 team with the KAST spectrograph on the Lick telescope) and three selected spectra from M. Shrestha et al. (2024). The inclusion of these external spectra is particularly valuable for analyzing the rapid spectral evolution during the earliest phases. For a number of spectra showing significant flux calibration discrepancies, adjustments were made by referencing multi-band photometric data. The first four spectra of SN 2023axu, obtained within 1.5 d after the explosion, exhibit a distinct “ledge-like” feature near 4600 Å. This feature had disappeared in the spectrum taken at  $t \approx 3.2$  d. Clear P-Cygni profiles subsequently developed, becoming evident approximately one week post-explosion.

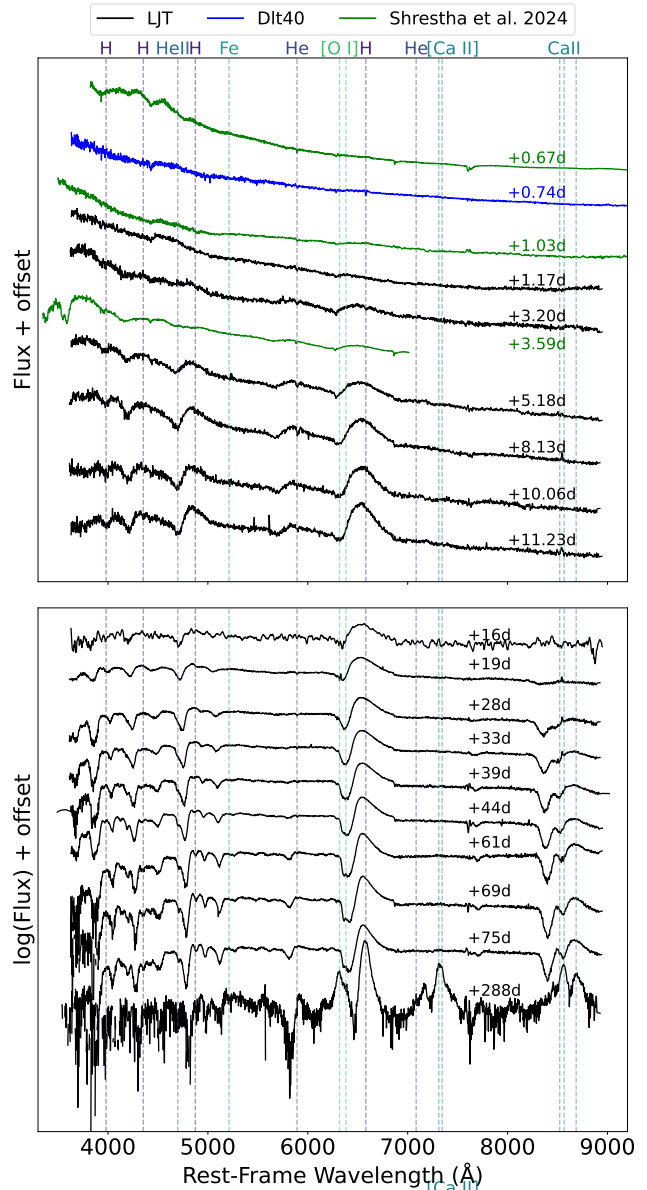


**Figure 3.** Spectra for SN 2023axu from +0.67 to +288 days after the explosion. All spectra have been vertically offset for clarity, with the epochs relative to the explosion date indicated on the right. Dashed lines in various colors mark the rest wavelengths of prominent spectral features for different elements. The spectra from LJT are marked in black, those from DLT40 in blue, and those from M. Shrestha et al. (2024) in green.

## 3. ANALYSIS AND RESULTS

### 3.1. Photometric Analysis

The early light curve of SN 2023axu shows a sharp rise in all optical bands. For example, it reaches the V-band peak at about 7 d after the explosion. Adopting the assumed distance to be  $13.68 \pm 2.05$  Mpc and the total extinction  $E(B - V)_{\text{total}} = 0.398 \pm 0.015$  mag de-

<sup>5</sup> ECSNOOPY is a package for SN photometry using PSF fitting and/or template subtraction developed by E. Cappellaro. A package description can be found at <http://sngroup.oapd.inaf.it/ecsnoopy.html>.

<sup>6</sup> <https://www.stsci.edu/hst/instrumentation/acs/data-analysis/zeropoints>

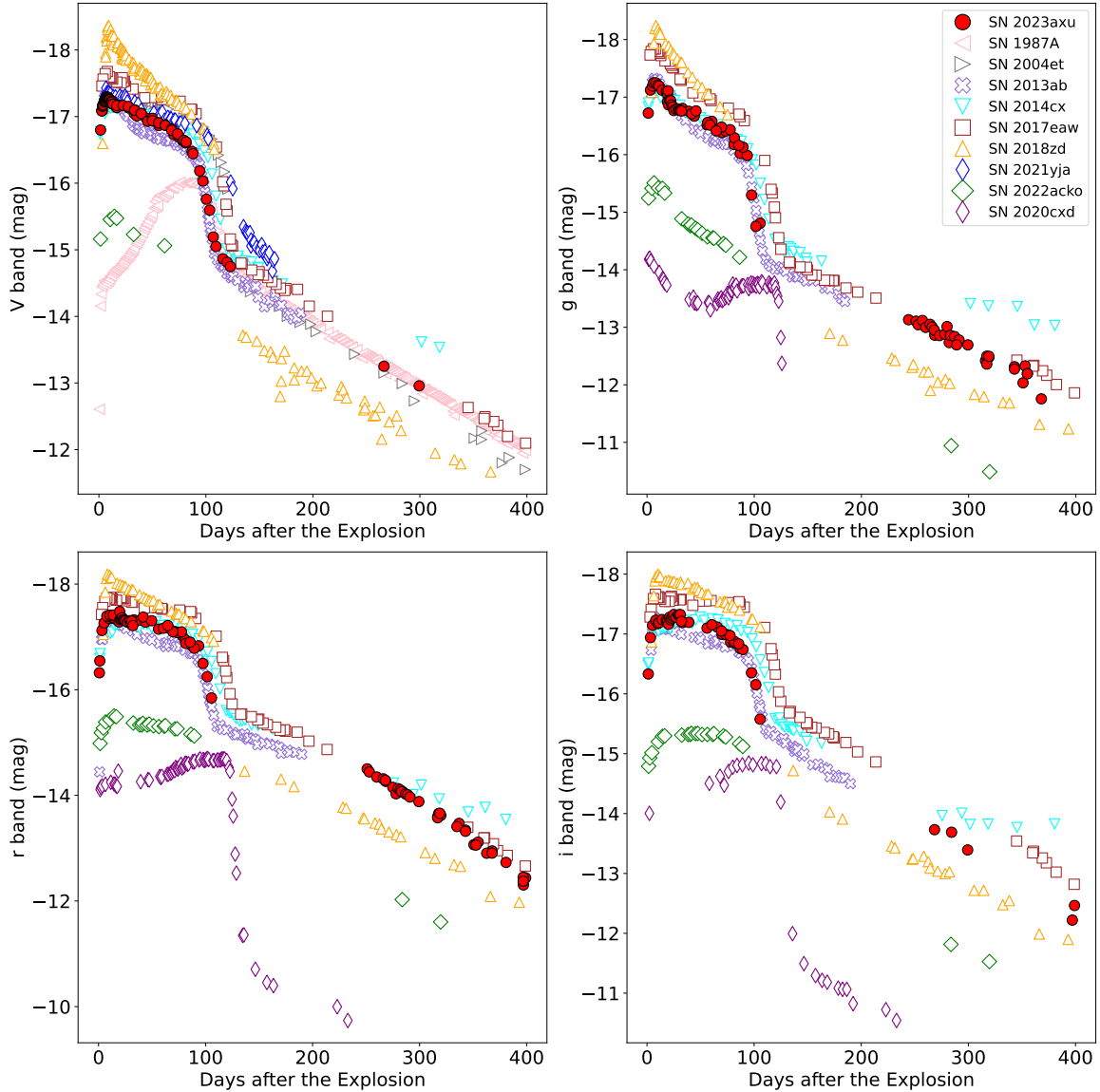


**Figure 4.** Absolute V, g, r, and i-band light curves of SN 2023axu compared with some well-studied SNe II.

rived by M. Shrestha et al. (2024), the V-band peak of SN 2023axu is  $M_V = -17.25 \pm 0.06$  mag. Subsequently, the V, r, i and z-band light curve has entered the plateau phase, sustained by hydrogen recombination, right after the peak at about 7 to 10 d after the explosion. Conversely, the g and B-bands exhibit a nearly linear decline rather than a clear plateau. At approximately 90 d after the explosion, the light curves across all bands entered a phase of rapid decline, signaling the end of the plateau phase and the beginning of the tail phase, which is primarily powered by the radioactive decay of synthesized  $^{56}\text{Ni}$ .

Figure 4 compares the light curve of SN 2023axu with those of several well-studied SNe II, including SNe 2017eaw (T. Szalai et al. 2019), 2018zd (J. Zhang

et al. 2020), 2020cxd (G. Valerin et al. 2022; Yang, S. et al. 2021), 2004et (K. Maguire et al. 2010), 2022acko (H. Lin et al. 2025), 2021yja (S. S. Vasylyev et al. 2022), 2014cx (F. Huang et al. 2016), and 2013ab (S. Bose et al. 2015). The light-curve evolution of SN 2023axu closely resembles that of typical SNe IIP, such as SNe 2017eaw, 2021yja, 2013ab, and 2014cx. This resemblance suggests that the energy source for SN 2023axu is similar to that of these events. During the nebular phase, the luminosity of SN 2023axu is lower than that of SN 2014cx and closer to that of SN 2017eaw in the i- and g-bands. However, in the r-band, the luminosities of these three SNe are similar.

In Figure 5, the  $g - r$  color of SN 2023axu was compared with that of a sample of SNe II. We found that

in the early stages post-explosion, SN 2023axu exhibited bluer colors than the comparison sample, resembling SN 2012A and SN 2017eaw. However, after approximately 60 days, the rate of color evolution slowed, causing the  $g-r$  color of SN 2023axu to converge towards that of the comparison SNe. In the late stages of the explosion, we observed that SN 2023axu became significantly redder, with a color decline steeper than that of SN 2018zd and comparable to SN 2017eaw. Overall, the color evolution of SN 2023axu is similar to that of SN 2017eaw, which also displays ledge feature in its early time spectra.

### 3.2. Bolometric Luminosity and Nickel Mass

Figure 6 displays the ultraviolet-optical-near-infrared pseudo-bolometric light curve of SN 2023axu, constructed by integrating the flux from the multi-band light curves presented in this work, along with the UV light curves obtained from *Swift* observations (M. Shrestha et al. 2024), using the SuperBol program<sup>7</sup> (M. Nicholl 2018). Additionally, the bolometric light curve is derived from these observations under the blackbody assumption. The bolometric luminosity peaks at  $L_{\max} = (3.8 \pm 0.3) \times 10^{42} \text{ erg s}^{-1}$  on MJD = 59978.3, approximately 7 d after the explosion, consistent with the optical light curve.

The radioactive-decay tail in SNe II is powered by the decay chain  $^{56}\text{Ni} \rightarrow ^{56}\text{Co} \rightarrow ^{56}\text{Fe}$ . Thus, a reliable indicator of the  $^{56}\text{Ni}$  mass produced in the explosion is the pseudo-bolometric luminosity. Equation (2) in M. Hamuy (2003) provides a method for calculating the mass of  $^{56}\text{Ni}$  by calculating the energy produced from the decay of  $^{56}\text{Ni}$ :

$$M_{\text{Ni}} = 7.866 \times 10^{-44} \times L_t \times \exp\left(\frac{(t - t_0)/(1+z) - 6.1}{111.26}\right) M_{\odot} \quad (2)$$

where  $t$  is the phase after explosion in days,  $L_t$  is the tail-phase luminosity in units of  $\text{ergs}^{-1}$ , and  $z$  is the redshift of the SN. We applied this method to estimate the mass of  $^{56}\text{Ni}$  produced by the explosion to be  $M_{\text{Ni}} = 0.058^{+0.017}_{-0.013} M_{\odot}$ , in excellent agreement with the value of  $0.058 M_{\odot}$  obtained via a similar method by M. Shrestha et al. (2024). This estimate is comparable to the nickel mass of  $0.056 \pm 0.008 M_{\odot}$  reported for SN 2014cx (F. Huang et al. 2016), consistent with the similar late-time light-curve evolution noted in Section 3.1.

For the effective calculation, we assume that the energy released by radioactive decay is fully captured, the deposited energy is re-emitted instantly, and no other

energy sources are present. However, we calculate that the pseudo-bolometric decline rate during this period is  $1.08 \text{ mag } 100 \text{ day}^{-1}$ , which is higher than the complete capture rate of  $^{56}\text{Co}$  decay, estimated at  $0.98 \text{ mag } 100 \text{ day}^{-1}$ . This indicates a loss from the energy generated by radioactive decay, so the actual mass of  $^{56}\text{Ni}$  produced could be higher than our calculated value.

We can also estimate the  $^{56}\text{Ni}$  mass from the nebula spectrum. A. Elmhamdi et al. (2003) noted a correlation between  $\text{H}\alpha$  intensity and nickel mass, and K. Maguire et al. (2012) provided the relation:

$$M_{\text{Ni}} = A \times 10^{B \times \text{FWHM}_{\text{corr}}} M_{\odot}, \quad (3)$$

where  $A = 1.8^{+1.0}_{-0.7} \times 10^{-3}$  and  $B = 0.023 \pm 0.004$ ,  $\text{FWHM}_{\text{corr}}$  is the full width at half-maximum intensity corrected for the instrumental broadening effect. Fitting the  $\text{H}\alpha$  of nebular spectrum of SN 2023axu ( $t \approx 288 \text{ d}$ ) gives  $\text{FWHM}_{\text{corr}} \approx 63.2 \text{ \AA}$ , yielding  $M_{\text{Ni}} = 0.05^{+0.02}_{-0.01} M_{\odot}$ , consistent with the value derived from late-time luminosity. By averaging the values derived from spectroscopic and photometric methods, we obtain a nickel mass estimate of  $M_{\text{Ni}} \approx 0.055 M_{\odot}$ .

### 3.3. Spectral Analysis

The most distinctive feature in the early-time spectra of SN 2023axu is a ledge-like, broad emission peak near  $4600 \text{ \AA}$ , which has been observed in only a handful of SNe II (J. E. Andrews et al. 2019; H. Lin et al. 2025; N. Rehemtulla et al. 2025; J. Pearson et al. 2023; Y. Murai et al. 2024). Figure 7 compares the early spectra of SN 2023axu (at  $t < 4 \text{ d}$ ) with those of other well-studied SNe II that exhibit ledge feature at similar phases, including SNe 2017eaw (T. Szalai et al. 2019), 2021yja (G. Hosseinzadeh et al. 2022), 1999gi (D. C. Leonard et al. 2002), 2018lab (J. Pearson et al. 2023), 2017gmr (J. E. Andrews et al. 2019), 2022acko (H. Lin et al. 2025), 2006bp (R. M. Quimby et al. 2007), and 2021gmj (Y. Murai et al. 2024). The ledge feature of SN 2023axu resembles those seen in SNe 2017eaw, 2006bp, and 2021yja.

The early spectra of SNe 2022acko and 2006bp showcase a narrow  $\text{H}\alpha$  emission line superimposed on a broad component. In contrast, no such feature is present in the early spectrum of SN 2023axu. A very faint  $\text{H}\alpha$  P-Cygni emission appeared in the spectrum 1.17 d post-explosion, with a velocity reaching  $15,000 \text{ km s}^{-1}$  derived from the absorption minimum. The ledge feature becomes faint in the spectrum taken 3.2 d post-explosion, while the hydrogen emission lines become clearer, maintaining a velocity around  $15,000 \text{ km s}^{-1}$ . Additionally, the  $\text{H}\beta$  and  $\text{H}\gamma$  lines are observed, also at velocities close to  $15,000 \text{ km s}^{-1}$ . If the ledge is considered to be the He II  $\lambda 4686$  emission line (C. Bullivant

<sup>7</sup> <https://github.com/mnicholl/superbol>

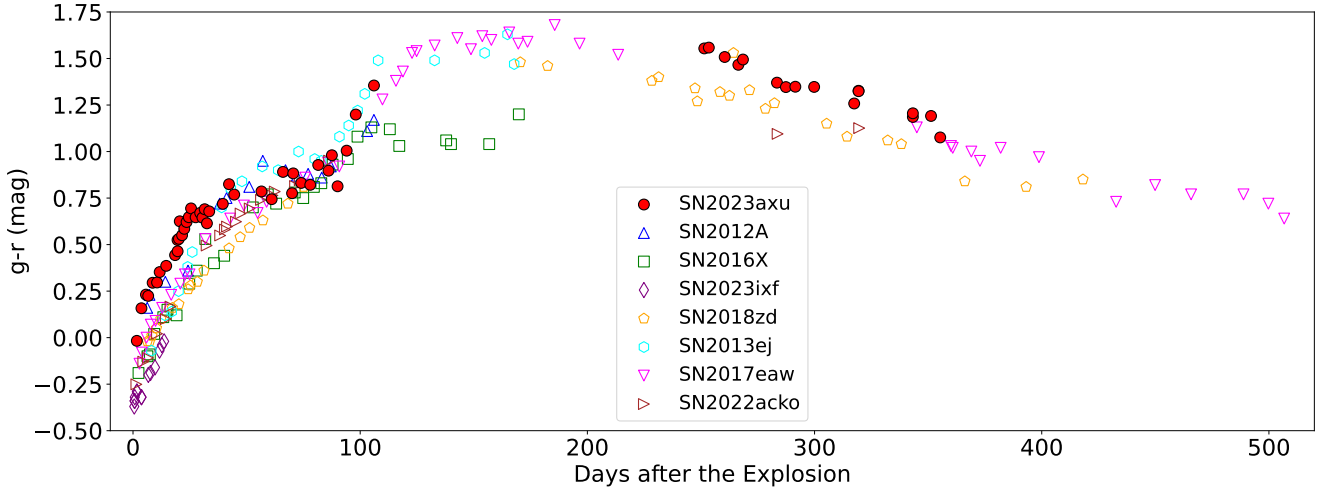


**Figure 5.** The  $g-r$  color curve evolution of SN 2023axu along with that of other well-studied.

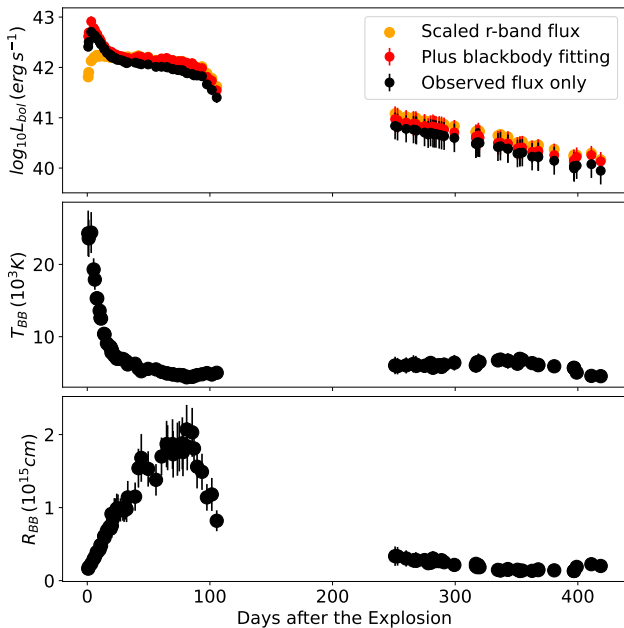


**Figure 6.** Bolometric light curve of SN 2023axu, including the pseudo-bolometric light curve (obtained by integrating the flux in the observed bands), the bolometric light curve derived from blackbody fitting and the r-band flux (scaled by its plateau flux match the calculated plateau flux of the pseudo-bolometric luminosity) as a reference. The middle panel presents the photospheric temperature from the blackbody fit, and the bottom panel shows the resulting photospheric radius, calculated from the bolometric luminosity and temperature. All quantities were derived using the `Superbol` code.

et al. 2018; J. E. Andrews et al. 2019), its velocity is approximately  $20,000 \text{ km s}^{-1}$ . A detailed discussion of the ledge feature in SN 2023axu is provided in Section 4.1.

Following the disappearance of the ledge feature, the spectra of SN 2023axu evolved into those typical of SNe IIP, characterized by P-Cygni profiles of hydrogen and helium superimposed on a cooling blackbody continuum. At  $t \sim 33 \text{ d}$ , the  $\text{H}\alpha$  absorption trough had expanded and developed a square-shaped profile. Concurrently, the overall P-Cygni profile widened, exhibiting a shallow absorption component at approximately  $10,000 \text{ km s}^{-1}$  of unknown origin. This feature, termed the “Cachito” (C. P. Gutiérrez et al. 2017), is located within the broad absorption structure. Subsequently, at  $t \sim 40 \text{ d}$ , metal lines such as Ba II and Fe II, along with various blends, became distinct in the spectra.

In Figure 8, we compare the late time spectra of SN 2023axu with SNe 2014cx (F. Huang et al. 2016), 2004et (T. Faran et al. 2014) and 1987A (C. S. Pun et al. 1995). We found that the late spectral features of SN 2023axu are more similar to those of SN 2014cx, while being weaker than those of SN 2004et and SN 1987A. The most noticeable difference is that the Na I P-Cygni profiles of SN 2023axu and SN 2014cx exhibit shallower absorption compared to the strong absorption seen in SN 2004et and SN 1987A. Additionally, the Ca II NIR triplet line emission is stronger in the latter two SNe (SN 2004et and SN 1987A), potentially indicating a higher degree of ionization.

### 3.4. Late Time Evolution

To gain deeper insights into the late-phase luminosity evolution of SN 2023axu, we accessed HST observations data at approximately 1000 d post-explosion from the MAST. From these data, we derived absolute fluxes to construct its spectral energy distribution (SED) at this epoch. Figure 9 presents this SED alongside contemporaneous SEDs of SN 1987A, SN 2004et and SN 2017eaw,

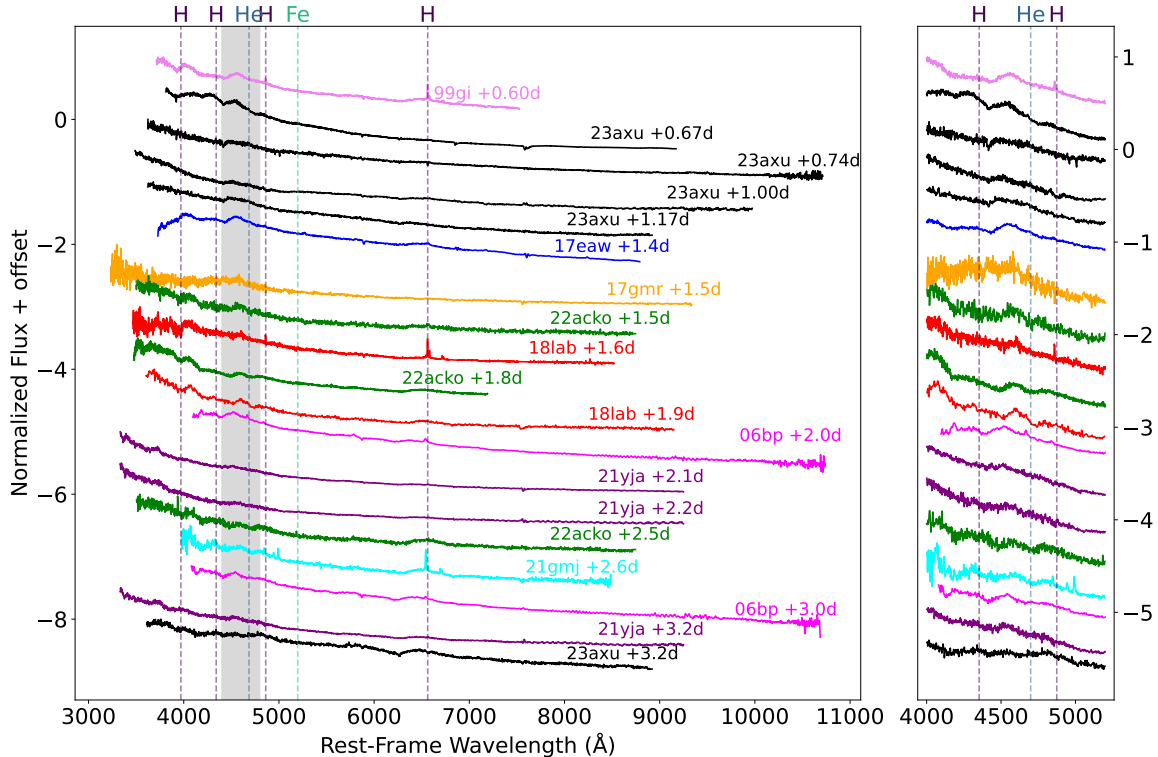


**Figure 7.** Left panel: Comparison of the early spectra of SN 2023axu with other well-studied SNe II exhibiting a similar ledge feature (marked in the gray shaded area in the left panel). Right panel: ledge feature present around 4600 Å.

showing that the SED of SN 2023axu closely resembles that of SN 1987A, whereas SN 2004et and SN 2017eaw exhibit brighter SED.

The F555W band is photometrically equivalent to the Johnson V-band, so we treated the F555W magnitudes as V-band measurements to compute the decline rate between 300 and 1000 d post-explosion. Over this interval, the late-time luminosity is dominated by the radioactive decay of  $^{56}\text{Co}$ . We derive a decline rate of  $1.08 \text{ mag } 100 \text{ d}^{-1}$  for SN 2023axu, significantly steeper than those of SN 2004et ( $0.83 \text{ mag } 100 \text{ d}^{-1}$ ) and SN 2017eaw ( $0.64 \text{ mag } 100 \text{ d}^{-1}$ ). Note that the rate for SN 2017eaw is measured over a longer baseline (300–1270 d), which may introduce additional uncertainty. Moreover, observational evidence indicates that the ejecta of SN 2017eaw interacted with pre-existing CSM at  $\sim 900$  d (K. E. Weil et al. 2020), which would flatten the late-time decline and thus affect the comparison.

However, a comparison the V- band light curves in Figure 4 shows that up to  $t \approx 400$  d the luminosity evolution of SN 2023axu closely tracks that of SN 2017eaw and SN 2004et, with an overall late-time decline rate near the  $^{56}\text{Co}$  decay rate ( $0.98 \text{ mag } 100 \text{ d}^{-1}$ ). This suggests that the differences in decline rates among these SNe emerges only after  $\sim 400$  d, i.e., within the latter portion of the 300–1000 day interval.

A plausible explanation for this divergence is sustained interaction with a circumstellar stellar wind. L. Dessart et al. (2023) presents radiative-transfer calculations for a SN II with and without such interaction, focusing on 350–1000 d after the explosion. In models without interaction, the ejecta are powered solely by radioactive decay, producing an exponential luminosity decline. In contrast, with continuous interaction against a steady wind, the contribution from radioactive decay diminishes beyond  $\sim 350$  d while the thermalized shock power from ejecta–CSM interaction grows, becoming dominant by  $\sim 1000$  d. This leads to a progressive flattening of the very-late-time light curve, as seen in SN 2017eaw and SN 2004et. The absence of comparable flattening in SN 2023axu therefore suggests minimal wind interaction at late times, making it a compelling example of a SN II with negligible late-time interaction power.

## 4. DISCUSSION

### 4.1. Origin of Ledge Feature

Explanations for the origin of the ledge feature are diverse but can be broadly classified into three categories. A. Pastorello et al. (2006) attributes this structure to high-velocity (HV)  $\text{H}\beta$ . However, our measurements of the Balmer line velocities (Figure 11) indicate a maxi-

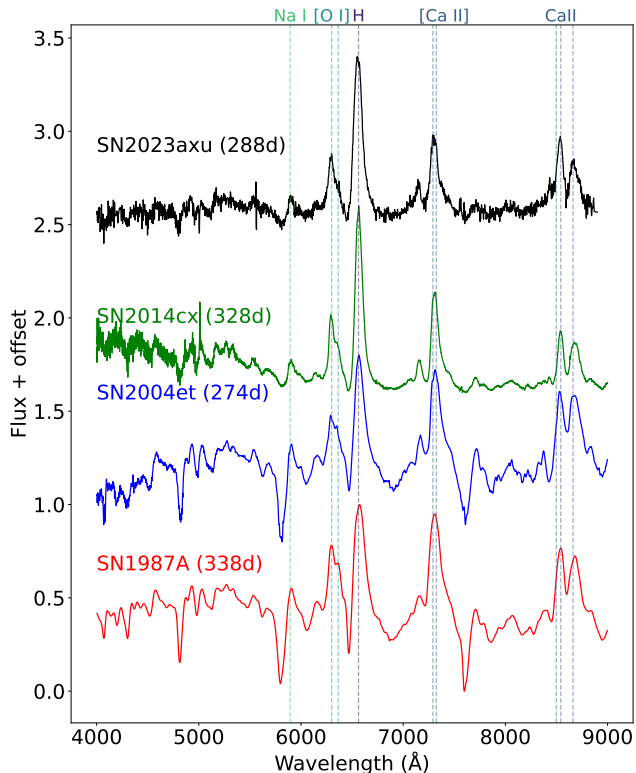


**Figure 8.** Comparison of the reddening- and Doppler-corrected spectra of SNe 2023axu, 2014cx, 2004et and 1987A obtained at about 300 d after the explosion.

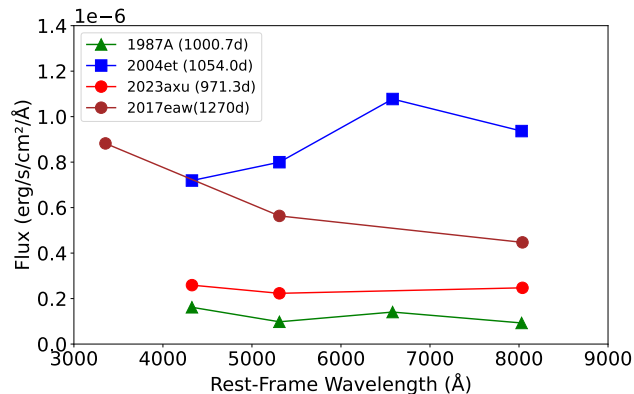


**Figure 9.** Late time SED of SN 2023axu with those of SN 1987A, SN 2004et, and SN 2017eaw at approximately 1000 d post-explosion. The SED of SN 2023axu is derived from HST photometry in the F438W, F555W, and F814W filters. In comparison, the data for SN 2017eaw is derived from HST photometry in the F336W, F555W, and F814W filters. Meanwhile, the photometric data for SN 2004et and SN 1987A are obtained in Johnson *BVRI*-bands. The data of SN 2017eaw is from S. D. Van Dyk et al. (2022), the data of SN 2004et is from K. Maguire et al. (2010), and the data of SN 1987A is from the Open Supernova Catalog<sup>a</sup> (J. Guillochon et al. 2017).

<sup>a</sup><https://github.com/astrocatalogs/supernovae>

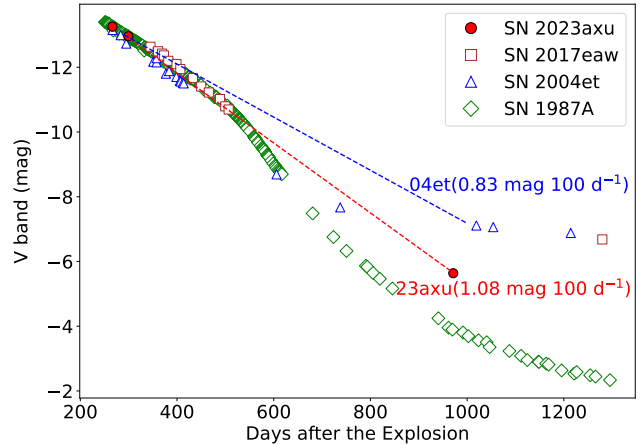


**Figure 10.** Comparison of the late-time absolute V-band light-curve evolution of SN 2023axu with SNe 2017eaw, 2004et, and 1987A. For reference, the decline rate of SN 2023axu and SN 2004et between 300 and 1000 d post-explosion is indicated with dashed lines.

imum hydrogen velocity of approximately  $15,000 \text{ km s}^{-1}$ . At 1 d after the explosion, when the ledge feature is clearly visible, it is difficult to precisely determine the velocities of the  $H\beta$  and  $H\gamma$  lines. Nevertheless, based on the velocity of the  $H\alpha$  line, they are unlikely to exceed  $20,000 \text{ km s}^{-1}$ . If the ledge feature were due to  $H\gamma$ , its velocity would need to be as high as  $30,000 \text{ km s}^{-1}$ , which significantly exceeds our observed values. We therefore do not favor this interpretation.

R. M. Quimby et al. (2007) suggest that this feature may instead arise from He II  $\lambda 4686$ , which would require high ionization in the outer ejecta layers. This interpretation has also been applied to SNe 2010id (A. Gal-Yam et al. 2011), 2017gmr (J. E. Andrews et al. 2019) and 2013fs (C. Bullivant et al. 2018). For example, the early spectrum of SN 2006bp exhibited narrow He II  $\lambda 4686$  emission with electron-scattering wings. Similar narrow emission features have been reported in other SNe such as SN 2013fs (C. Bullivant et al. 2018). However, no such feature is present in the early spectra of SN 2023axu.

A third explanation posits that the ledge consists of broad lines produced by bulk motion, blended with several ionized features from CSM (G. Hosseinzadeh et al. 2018, 2022; M. T. Soumagnac et al. 2020; R. J. Bruch et al. 2021). The feature may be a blend of ions such as N V, N III, C III, O III, and He II; approximate velocities for these lines are indicated in Figure 11. Narrow emission lines with electron-scattering wings result from non-coherent scattering by thermal electrons, whereas bulk motion can produce broad, blended spectral features (L. Dessart et al. 2009). However, as noted by G.

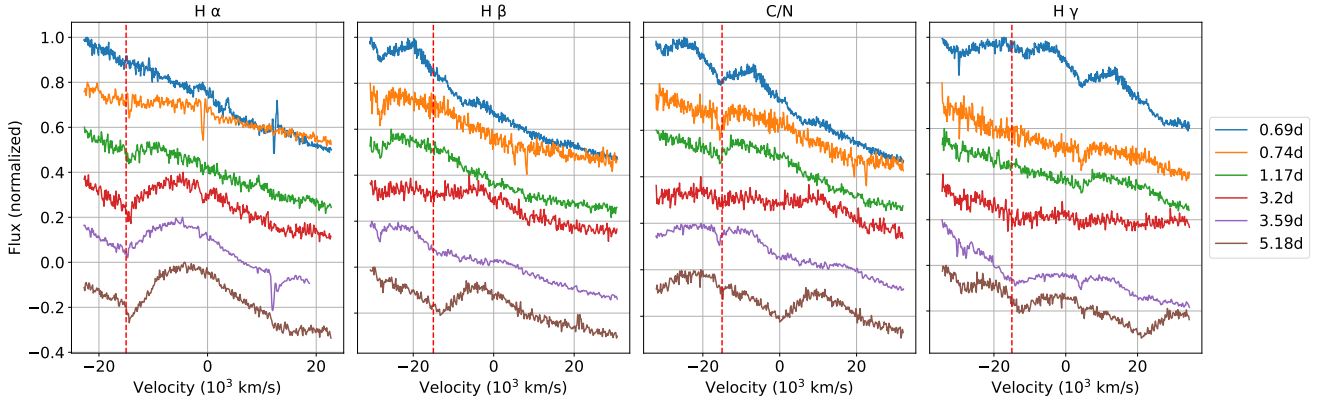


**Figure 11.** The measurement of emission line velocities in the early spectra of SN 2023axu included the Balmer emission lines of H and the group of C III and N III emission lines (with  $\lambda 4645 \text{ \AA}$  selected for measurement), all spectra were normalized. The red dashed line indicating a velocity of  $15,000 \text{ km s}^{-1}$  as a reference. There is an atmospheric absorption line near the  $H\alpha$  line at  $6280 \text{ \AA}$ , which coincides closely with the position of its minimum absorption. Although there is still a slight effect after atmospheric extinction correction, it does not affect the judgment of its velocity.

Hosseinzadeh et al. (2022), the breadth and strength of the ledge may be inconsistent with an origin in multiple narrow emission lines.

We also compare SN 2023axu with the synthetic spectra from the multi-group radiation-hydrodynamics and non-LTE radiative transfer models of L. Dessart et al. (2017). These models depend on three key parameters: the initial RSG radius ( $r$ ), the wind mass-loss rate ( $w$ ), and the presence of an extended atmospheric envelope ( $h$ ). J. Pearson et al. (2023) and G. Hosseinzadeh et al. (2022) matched observed spectra with models r1w1h and r1w5h, suggesting that an RSG exploding into a low-density CSM with an extended atmosphere can account for the early spectra of SN 2018lab and SN 2021yja. In Figure 12, we compare the early spectra of SN 2023axu with the L. Dessart et al. (2017) models (r1w1, r1w1h, and r1w5h). The spectrum at 0.67 d is not well reproduced by any model, as it shows additional broad features between  $4000$  to  $4400 \text{ \AA}$  that are absent from the model grid. By contrast, the spectra at 0.74, 1.03, and 1.17 d most closely resemble the r1w1 model at 1.0 d and the r1w1h model at 1.6 d, consistent with M. Shrestha et al. (2024). However, r1w1h predicts narrow emission lines at early times that are not observed in SN 2023axu. Furthermore, our comparison with the pseudo-bolometric light curve in Section 4.2 indicates that r1w1 provides a better match. We therefore favor r1w1 as the best overall fit, although we cannot entirely rule out the presence of weak, undetected narrow features in the earliest spectrum.

Regarding whether the ledge feature results from a blend of multiple emission lines, H. Lin et al. (2025) note that  $H\alpha$  should also show a characteristic narrow emission component with electron-scattering wings—a feature absent in SN 2023axu and many other SNe. The

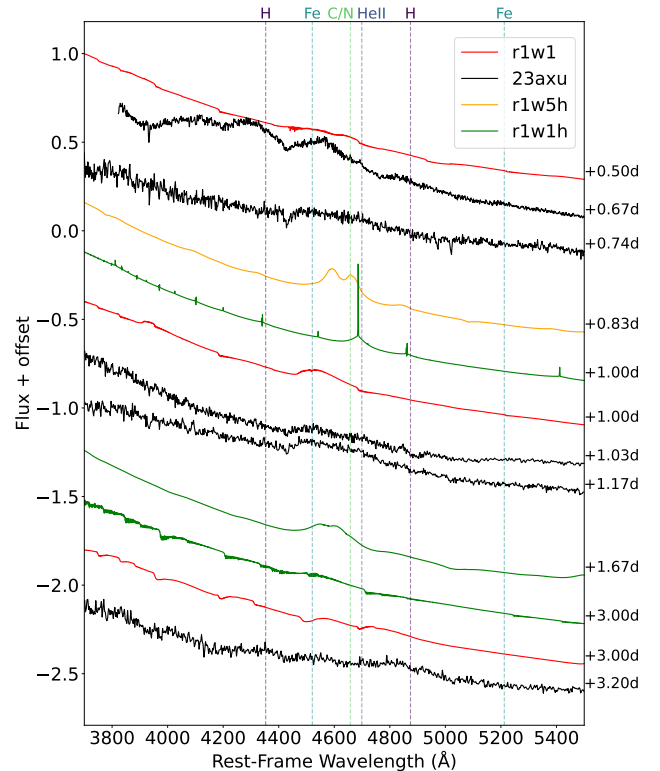


**Figure 12.** Comparison of the early spectra of SN 2023axu with the r1w1, r1w1h, r1w5h model spectrum from L. Dessart et al. (2017). The r1w1 and r1w1h model have a wind mass loss rates of  $10^{-6} M_{\odot} \text{ yr}^{-1}$  while r1w5h model has a wind mass loss rates of  $5 \times 10^{-3} M_{\odot} \text{ yr}^{-1}$ , The r1w1h and model include an extended RSG atmosphere of  $H_{\rho} = 0.3 R_{\star} = 150.3 R_{\odot}$ , and the r1w5h model's atmosphere is  $H_{\rho} = 0.1 R_{\star} = 50.1 R_{\odot}$ , where  $R_{\star}$  is the radius of RSG.

shape of ledge in SN 2023axu more closely resembles that of SNe 2017eaw and 2021yja, appearing similar to a P-Cygni profile. Furthermore, at  $t \sim 0.67$  d, broad emis-

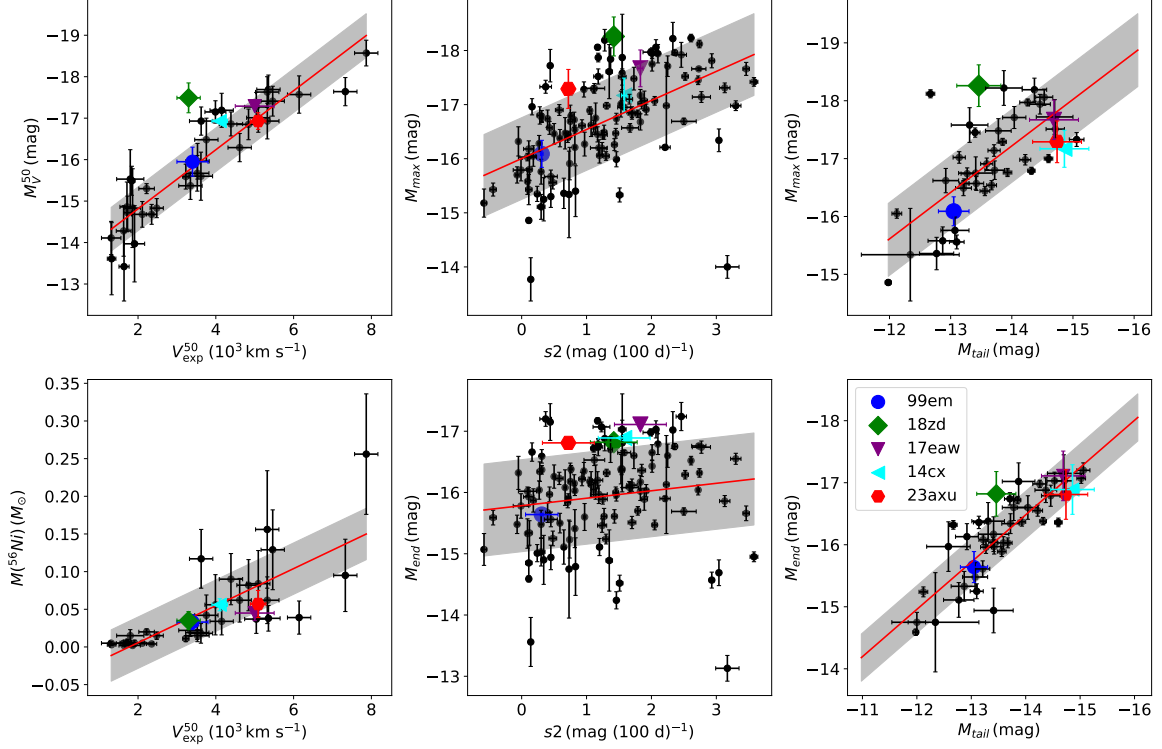


**Figure 13.** Photometric and spectroscopic parameter space for SNe II, showing the position of SN 2023axu relative to a literature sample (M. Hamuy 2003; J. P. Anderson et al. 2014; S. Spiro et al. 2014; J. Zhang et al. 2014). Parameters include the V-band absolute magnitude measured at around 50 d after explosion ( $M_V^{50}$ ), the expansion velocity of Fe II  $\lambda$  5169 measured at 50 d after the explosion ( $v_{exp}^{50}$ ), the mass of  $^{56}\text{Ni}$ , three shape parameters of the V-band light curve defined by J. P. Anderson et al. (2014) ( $M_{max}$ ,  $M_{end}$ ,  $M_{tail}$ ), and the decline rate of the plateau ( $s2$ ). Individual SNe (1999em, 2018zd, 2017eaw, 2014cx) are highlighted. The red line and gray band show the linear fit and its  $1\sigma$  uncertainty.

sion features appeared in the 4000–4400 Å range, similar to those seen in later spectra. We conclude that these features originate from the outer ejecta. Under rapid expansion, the optical depth of the ejecta changes quickly. Initially, the outer layers are transparent, allowing high-energy spectral lines to appear briefly; within hours, the inner layers become optically thick, causing these emission features to vanish. This rapid evolution also supports the view that the CSM around SN 2023axu is very tenuous, unable to absorb these photons efficiently. The features disappear in the subsequent spectrum taken at 0.74 d, just hours later.

We therefore support the view of H. Lin et al. (2025) and L. Dessart et al. (2008) that the ledge of SN 2023axu is a P-Cygni feature originating from ionized ejecta—not from flash-ionized unshocked CSM. H. Lin et al. (2025) proposes that the ledge feature is blueshifted He II  $\lambda$  4686 for SN 2022acko, produced by high-energy photons arising from the CSI of SN ejecta which produced high-ionization species. The spectral lines originating from the ionized SN ejecta will exhibit distinct line shapes and velocities compared to those from the CSM, resulting in such a broad feature. The He II  $\lambda$  4686 line veloc-

ity of 2022acko is close to its hydrogen line, supporting the above conclusion. But as noted in section 3.3, the ledge of SN 2023axu is more blueshifted, resulting in a higher He II velocity, while the velocities that match better should be those of C III  $\lambda$  4647 and N III  $\lambda$  4638 lines as seen in Figure 11. Therefore, the ledge feature of SN 2023axu should be result from the overlapping emission features of C III  $\lambda$  4647, N III  $\lambda$  4638, and He II  $\lambda$  4686 lines.

We propose the physical mechanism underlying formation of the entire ledge feature: During the progenitor phase, minimal mass loss results in the absence of a dense CSM shell. The sparse ejected material remains confined near the progenitor system. Following the SN explosion, the rapidly expanding ejecta interact with this tenuous material, ionizing and accelerating it to extreme velocities (potentially including the progenitor’s outer layers). This interaction generates the observed ledge feature, explaining both its Doppler broadening and high-velocity characteristics. Furthermore, the weak-wind scenario implied by the ledge feature is supported by the late-time photometric decline rate and the absence of clear wind-interaction signatures

(Section 3.4), together indicating that the progenitor of SN 2023axu did not sustain a strong wind capable of producing a dense CSM.

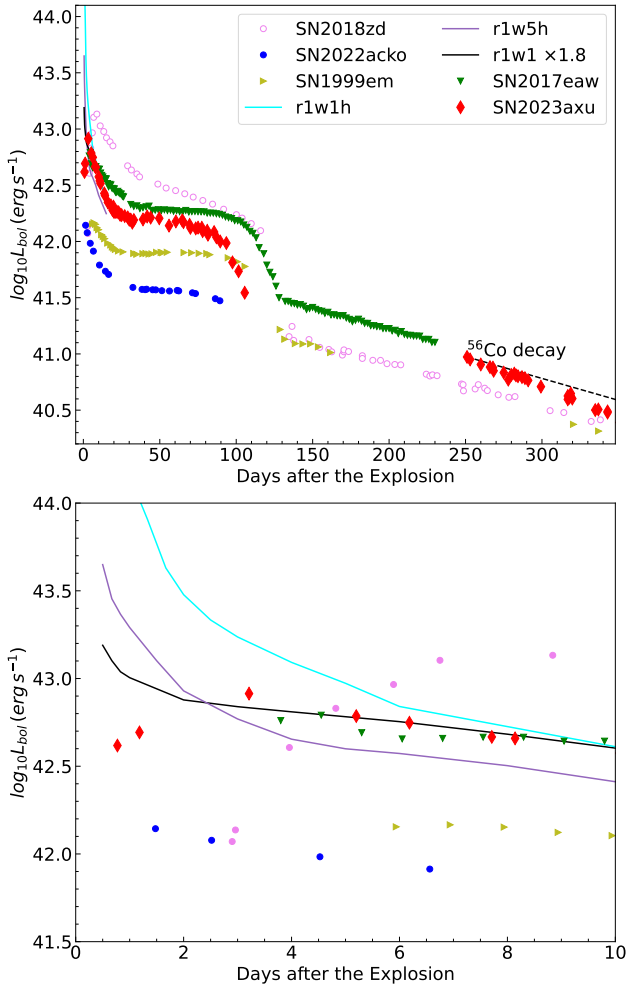


**Figure 14.** Pseudo-bolometric light curve compared with that of a few well-studied SNe II and the model bolometric light curve in the L. Dessart et al. (2017).

#### 4.2. Weak Stellar Wind Interaction of SNe II

To contextualize SN 2023axu within the population of SNe II, we compare its spectral and photometric parameters with those of well-studied SNe II from the literature (M. Hamuy 2003; J. P. Anderson et al. 2014; S. Spiro et al. 2014; J. Zhang et al. 2014), as well as with individual objects: the normal SNe II 2014cx and 1999em, the ledge-feature SN 2017eaw, and the flash-ionized SN 2018zd. The comparison, illustrated in Figure 13, reveals the following:

(1) SN 2023axu and SN 2017eaw, which exhibit ledge features, are brighter by  $0.75 \pm 0.5$  mag at peak ( $M_{max}$ ) and in the tail ( $M_{tail}$ ) compared to SNe samples with a

similar decline rate of s2 (J. P. Anderson et al. 2014). However, their middle plateau ( $M_V^{50}$ ) are consistent with those of SNe having comparable ejecta expansion velocities ( $v_{exp}^{50}$ ).

(2) The luminosity decline from peak to tail is more gradual in SN 2023axu and SN 2017eaw than in the sample average, being slightly lower and closer to that of typical SNe II, such as SN 2014cx. In contrast, SN 2018zd, which exhibits flash-ionized emission lines, experiences a significant luminosity drop from peak to tail (J. Zhang et al. 2020).

A similar trend is seen in the light-curve comparison in Figure 4: the ledge-sample objects closely resemble ordinary SNe II, whereas flash-ionized events like SN 2018zd show higher early peak luminosity and a steeper pre-plateau decline. This is expected if flash features arise from CSM interaction, where a substantial fraction of kinetic energy is converted into radiation via strong ejecta–wind collision. The luminosity of SN 2023axu at various phases resembles that of normal SNe II, and its decline rate is relatively slow. This suggests that the efficiency of converting kinetic energy into radiation within the ionized ejecta is low, with only a small fraction of kinetic energy being thermalized, yielding negligible optical brightening.

The light-curve evolution of SN 2023axu stands in sharp contrast to SNe interacting with dense CSM, such as SN 2018zd. The latter typically show narrow emission lines, sustained early brightness, and light-curve shapes resembling SNe IIL. To elucidate the luminosity evolution of SN 2023axu, we compared its pseudo-bolometric light curve with other well-studied SNe II samples and model bolometric light curves from L. Dessart et al. (2017) in Figure 14. While pseudo-bolometric estimates can be affected by band coverage and the non-blackbody nature of SNe, and the L. Dessart et al. (2017) models are idealized and may not map one-to-one onto observations, the r1w1 model bolometric light curve nonetheless closely matches the pseudo-bolometric light curve of SN 2023axu. This agreement further supports r1w1 as the preferred model for SN 2023axu.

Combining our analysis with the model light curve, we note that the strength of CSM interaction is tied to the mass-loss history of the progenitor star. Strong stellar winds (e.g., models r1w4, r1w6) produce a dense, extended CSM, leading to vigorous interaction that efficiently thermalizes kinetic energy into radiation—manifested as early brightening, linear declines (IIL-like), and flash spectral features. SN 2023axu, instead, exemplifies the weak-wind scenario (e.g., r1w1): its low-density CSM leads to very weak interaction, min-

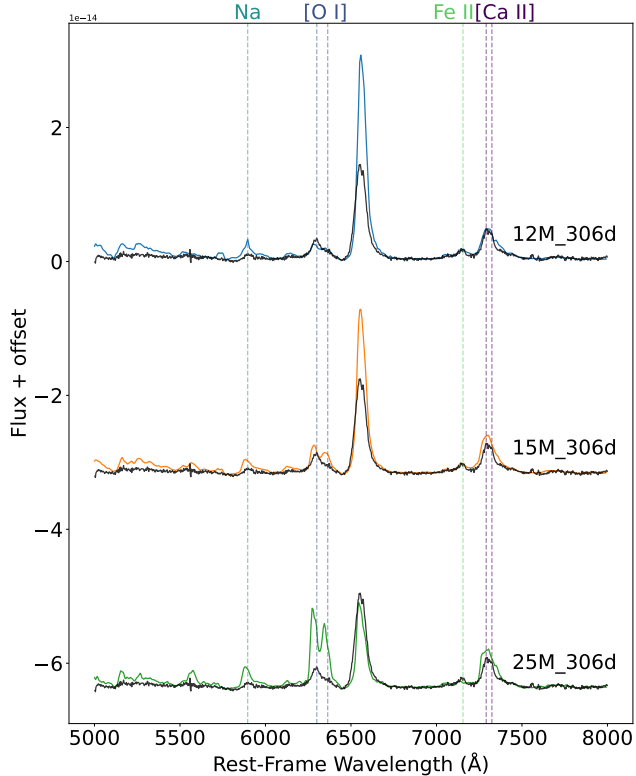


**Figure 15.** Comparison of nebular spectra of SN 2023axu at  $t \approx 288$  d with the 306 d model spectrum from A. Jerkstrand et al. (2012); A. Jerkstrand et al. (2014). All model spectra were scaled to match the distance of SN 2023axu. The black line in the figure represents the nebular spectrum of SN 2023axu, while the spectra in other colors are model spectra for different progenitor masses and spectral phases.

imal conversion of kinetic energy to radiation, and a light curve that closely follows that of a normal SN IIP.

#### 4.3. Progenitor Mass

The nebular-phase spectrum of SN 2023axu ( $t \sim 288$  d) allows us to estimate the properties of its progenitor star. A common approach is to use the flux of the [O I]  $\lambda\lambda$  6300,6364 doublet as a proxy for the CO core mass, which in turn reflects the progenitor mass (A. Jerkstrand et al. 2014; A. Uomoto 1986). However, the absolute flux is sensitive to uncertainties in distance and extinction. More robust indicators involve using the relative flux of the [O I] doublet, either normalized to the 5000–8500 Å continuum (Q. Fang et al. 2025) or compared to the [Ca II]  $\lambda\lambda$  7291, 7324 doublet (C. Fransson & R. A. Chevalier 1989; Q. Fang et al. 2022), as these ratios are less sensitive to systematic uncertainties.

We compare the nebular spectrum of SN 2023axu with theoretical models from A. Jerkstrand et al. (2012); A. Jerkstrand et al. (2014) in Figure 15, which link spectral features to progenitor masses under the assumption

of a retained hydrogen-rich envelope. In the figure, we overplot the 306 d model because it is closer in phase to our observation than the 250 d model and provides a notably better match to the continuum. The observed H $\alpha$  emission is significantly weaker than predicted by these models, this discrepancy likely results from substantial mass loss before explosion: hydrodynamic simulations show that SNe II with stripped hydrogen envelopes ( $M_{Henv} < 3 M_{\odot}$ ) exhibit suppressed H $\alpha$  flux due to lower recombination efficiency, while other spectral regions are less affected (Dessart, Luc & John Hillier, D. 2020; Q. Fang et al. 2025). Observations support this trend — SNe II showing plateau light curves indicative of low  $M_{Henv}$  consistently display faint nebular H $\alpha$  lines (Q. Fang et al. 2024; R. S. Teja et al. 2022, 2023; A. P. Ravi et al. 2025). Although CSM interaction could enhance H $\alpha$  emission, spectroscopic analysis of SN 2023axu suggests minimal CSM interaction, ruling out this mechanism as a significant contributor (Dessart, Luc et al. 2023).

From the comparison in Figure 15, the 12  $M_{\odot}$  and 15  $M_{\odot}$  progenitor models at 306 d post-explosion show the best agreement with the observed flux ratio of [O I] to [Ca II]. We performed Gaussian fitting on the nebular spectrum (Figure 16) to measure these fluxes, obtaining a ratio of 0.61 for SN 2023axu. The same method applied to the 12  $M_{\odot}$  and 15  $M_{\odot}$  models at 306 d yields ratios of 0.49 and 0.68, respectively, supporting a progenitor mass between 12 – 15  $M_{\odot}$ .

We also applied the diagnostic of Q. Fang et al. (2025), which uses the ratio of the [O I]  $\lambda\lambda$  6300,6364 doublet flux to the integrated flux within 5000–8500 Å as a progenitor-mass indicator. To mitigate potential contamination, we subtracted the H $\alpha$  contribution from the total. The derived relative flux for SN 2023axu is 0.194. This value is significantly higher than that of the 12  $M_{\odot}$  model at 306 d (0.104) and closely matches the 15  $M_{\odot}$  model at the same epoch (0.198), further supporting a progenitor mass closer to 15  $M_{\odot}$ . We note that this result carries uncertainties, primarily from continuum flux estimation. Furthermore, all calculations rule out a high-mass progenitor at  $M_{ZMAS} \geq 19 M_{\odot}$ .

We also noted that the Na  $\lambda\lambda$  5890,5896 line emission of SN 2023axu is significantly weaker than in the model. Although sodium nucleosynthesis does not vary monotonically with progenitor mass, this may also indicate hydrogen envelope stripping. In contrast, the Fe II  $\lambda$  7155 line intensity matches the models, suggesting that sodium exists in a highly ionized state. Given the low temperatures in the nebular phase, this could be due to a reduced recombination rate caused by very low density in the late-time ejecta.

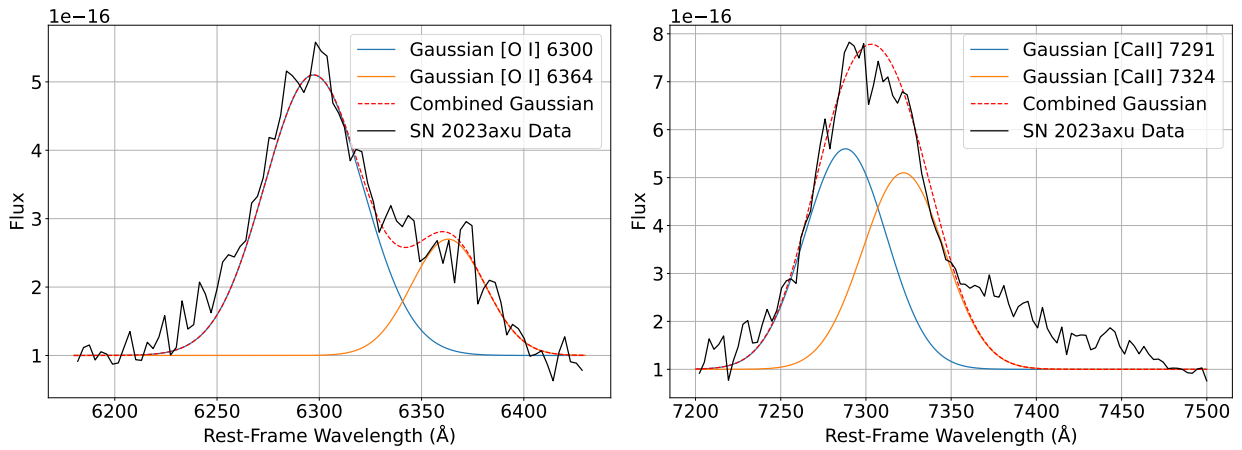


**Figure 16.** Gaussian fitting of the [O I]  $\lambda\lambda 6300, 6364$  lines and [Ca II]  $\lambda\lambda 7291, 7324$  lines in the nebular spectrum of SN 2023axu.

## 5. CONCLUSIONS

SN 2023axu reached a peak absolute  $V$ -band magnitude of  $M_V = -17.25 \pm 0.06$  at about 7 d after the explosion, and produced about  $0.055 M_\odot$  of  $^{56}\text{Ni}$ . Combining constraints from nebular spectral modeling and emission-line ratios, we estimate a progenitor mass about  $15 M_\odot$ .

The spectral evolution of SN 2023axu is largely consistent with that of typical SNe IIP, though it shows a distinct broad “ledge” feature near  $4600 \text{ \AA}$  in early phases. We have investigated the origin of this feature by comparing SN 2023axu with other SNe and with the spectral models of [L. Dessart et al. \(2017\)](#), the early-time spectra are best reproduced by the weak-wind model (r1w1). The presence of additional broad emission features in the 0.67 d spectrum, along with the P-Cygni-like morphology of the ledge, supports the interpretation by [H. Lin et al. \(2025\)](#) that the ledge is a P-Cygni profile formed in the ionized ejecta and sparse mass loss material remains confined near the SN. In the case of SN 2023axu, the feature likely arises from a blend of C, N, and He lines, rather than He alone. Furthermore, the late-time photometric decline rate approaches the  $^{56}\text{Co}$  decay rate, and the absence of discernible interaction power indicates no strong late-time interaction, consistent with the weak-wind scenario.

Comparison with well-studied SNe shows that the light curve of SN 2023axu is consistent with those of normal SNe IIP. SNe with early flash-ionized emission lines, such as SN 2018zd, typically exhibit steeper post-peak declines, resembling the IIL subtype. This divergence can be understood within the framework of [L. Dessart et al. \(2017\)](#), which links the mass-loss history of the progenitor to the observed light-curve shape. Progenitors with high mass-loss rates develop dense CSM; the resulting strong ejecta–CSM interaction efficiently con-

verts kinetic energy into radiation, leading to rapidly declining light curves and flash-ionized spectral features. SN 2023axu, on the other hand, exemplifies the weak-wind scenario: its tenuous CSM leads to minimal interaction, little additional thermalization of kinetic energy, and a light curve closely matching those of typical SNe IIP.

In summary, the multi-wavelength analysis of SN 2023axu contributes to our understanding of the ledge feature and exemplifies the weak mass-loss pathway that leads to minimal CSM interaction, thereby helping to explain the observed divergence in light-curve evolution between SNe IIP and IIL.

## ACKNOWLEDGMENTS

This work is supported by the B-type Strategic Priority Program of the Chinese Academy of Sciences (Grant No. XDB1160202), the National Key R&D Program of China with grant 2021YFA1600404, the National Natural Science Foundation of China (NSFC grants 12173082 and 12333008), the Yunnan Fundamental Research Projects (YFRP; grants 202501AV070012 and 202401BC070007), the Top-notch Young Talents Program of Yunnan Province, the Light of West China Program provided by the Chinese Academy of Sciences, and the International Centre of Supernovae (ICE-SUN), Yunnan Key Laboratory of Supernova Research (No. 202505AV340004). AP, AR, GV acknowledge support from the PRIN-INAF 2022, “Shedding light on the nature of gap transients: from the observations to the models”. AR also acknowledges financial support from the GRAWITA Large Program Grant (PI P. D’Avanzo). Yongzhi Cai is supported by the National Natural Science Foundation of China (NSFC, Grant No. 12303054), the National Key Research and Development Program of China (Grant No. 2024YFA1611603), the

Yunnan Fundamental Research Projects (Grant Nos. 202401AU070063, 202501AS070078). We acknowledge the support of the staff of the LJT. Funding for the LJT has been provided by the CAS and the People's Government of Yunnan Province. The LJT is jointly operated and administrated by YNAO and Center for Astronomical Mega-Science, CAS. This article is also based on observations made with the Rapid Eye Mount Telescope, operated in La Silla by INAF under the pro-

gram A47TAC\_37 (PI: G. Valerin). Based on observations collected at Schmidt 67/92 telescope (Asiago Mount Ekar, Italy) of the INAF - Osservatorio Astronomico di Padova.

**Facilities:** YAO:2.4m (LJT), WMS, REM, Schmidt 67/92 telescopes.

**Software:** PyRAF ([Science Software Branch at STScI 2012](#)), NumPy ([C. R. Harris et al. 2020](#)), Matplotlib ([J. D. Hunter 2007](#)).

## REFERENCES

- Anderson, J. P., González-Gaitán, S., Hamuy, M., et al. 2014, *The Astrophysical Journal*, 786, 67, doi: [10.1088/0004-637X/786/1/67](#)
- Andrews, J. E., Sand, D. J., Valenti, S., et al. 2019, *The Astrophysical Journal*, 885, 43, doi: [10.3847/1538-4357/ab43e3](#)
- Bose, S., Valenti, S., Misra, K., et al. 2015, *Monthly Notices of the Royal Astronomical Society*, 450, 2373, doi: [10.1093/mnras/stv759](#)
- Bostroem, K. A., Pearson, J., Shrestha, M., et al. 2023a, *ApJL*, 956, L5, doi: [10.3847/2041-8213/acf9a4](#)
- Bostroem, K. A., Brink, T. G., Filippenko, A. V., et al. 2023b, *Transient Name Server Classification Report*, 2023-230, 1
- Bruch, R. J., Gal-Yam, A., Schulze, S., et al. 2021, *The Astrophysical Journal*, 912, 46, doi: [10.3847/1538-4357/abef05](#)
- Bruch, R. J., Gal-Yam, A., Yaron, O., et al. 2023, *The Astrophysical Journal*, 952, 119, doi: [10.3847/1538-4357/acd8be](#)
- Bullivant, C., Smith, N., Williams, G. G., et al. 2018, *MNRAS*, 476, 1497, doi: [10.1093/mnras/sty045](#)
- Dessart, L., Gutierrez, C. P., Kuncarayakti, H., Fox, O. D., & Filippenko, A. V. 2023, *Astronomy & Astrophysics*, 675, A33
- Dessart, L., Hillier, D. J., Gezari, S., Basa, S., & Matheson, T. 2009, *Monthly Notices of the Royal Astronomical Society*, 394, 21, doi: [10.1111/j.1365-2966.2008.14042.x](#)
- Dessart, L., John Hillier, D., & Audit, Edouard. 2017, *A&A*, 605, A83, doi: [10.1051/0004-6361/201730942](#)
- Dessart, L., Blondin, S., Brown, P. J., et al. 2008, *The Astrophysical Journal*, 675, 644, doi: [10.1086/526451](#)
- Dessart, Luc, Gutiérrez, Claudia P., Kuncarayakti, Hanindyo, Fox, Ori D., & Filippenko, Alexei V. 2023, *A&A*, 675, A33, doi: [10.1051/0004-6361/202345969](#)
- Dessart, Luc, & John Hillier, D. 2020, *A&A*, 642, A33, doi: [10.1051/0004-6361/202038148](#)
- Elmhamdi, A., Danziger, I. J., Chugai, N., et al. 2003, *MNRAS*, 338, 939, doi: [10.1046/j.1365-8711.2003.06150.x](#)
- Fan, Y.-F., Bai, J.-M., Zhang, J.-J., et al. 2015, *Research in Astronomy and Astrophysics*, 15, 918, doi: [10.1088/1674-4527/15/6/014](#)
- Fang, Q., Moriya, T. J., & Maeda, K. 2025, *ApJ*, 986, 39, doi: [10.3847/1538-4357/adceae](#)
- Fang, Q., Maeda, K., Kuncarayakti, H., et al. 2022, *ApJ*, 928, 151, doi: [10.3847/1538-4357/ac4f60](#)
- Fang, Q., Moriya, T. J., Ferrari, L., et al. 2024, *The Astrophysical Journal*, 978, 36, doi: [10.3847/1538-4357/ad8d5a](#)
- Faran, T., Poznanski, D., Filippenko, A. V., et al. 2014, *Monthly Notices of the Royal Astronomical Society*, 442, 844, doi: [10.1093/mnras/stu955](#)
- Fransson, C., & Chevalier, R. A. 1989, *ApJ*, 343, 323, doi: [10.1086/167707](#)
- Gal-Yam, A., Kasliwal, M. M., Arcavi, I., et al. 2011, *The Astrophysical Journal*, 736, 159, doi: [10.1088/0004-637X/736/2/159](#)
- Gal-Yam, A., Arcavi, I., Ofek, E. O., et al. 2014, *Nature*, 509, 471, doi: [10.1038/nature13304](#)
- Guillochon, J., Parrent, J., Kelley, L. Z., & Margutti, R. 2017, *The Astrophysical Journal*, 835, 64, doi: [10.3847/1538-4357/835/1/64](#)
- Gutiérrez, C. P., Anderson, J. P., Hamuy, M., et al. 2017, *ApJ*, 850, 89, doi: [10.3847/1538-4357/aa8f52](#)
- Hamuy, M. 2003, *ApJ*, 582, 905, doi: [10.1086/344689](#)
- Harris, C. R., Millman, K. J., van der Walt, S. J., et al. 2020, *Nature*, 585, 357, doi: [10.1038/s41586-020-2649-2](#)
- Heger, A., Fryer, C. L., Woosley, S. E., Langer, N., & Hartmann, D. H. 2003, *The Astrophysical Journal*, 591, 288, doi: [10.1086/375341](#)
- Hosseinzadeh, G., Valenti, S., McCully, C., et al. 2018, *The Astrophysical Journal*, 861, 63, doi: [10.3847/1538-4357/aac5f6](#)
- Hosseinzadeh, G., Kilpatrick, C. D., Dong, Y., et al. 2022, *The Astrophysical Journal*, 935, 31, doi: [10.3847/1538-4357/ac75f0](#)

- Huang, F., Wang, X., Zampieri, L., et al. 2016, *The Astrophysical Journal*, 832, 139, doi: [10.3847/0004-637X/832/2/139](https://doi.org/10.3847/0004-637X/832/2/139)
- Hunter, J. D. 2007, *Computing in Science & Engineering*, 9, 90, doi: [10.1109/MCSE.2007.55](https://doi.org/10.1109/MCSE.2007.55)
- Jacobson-Galán, W. V., Dessart, L., Davis, K. W., et al. 2024, *ApJ*, 970, 189, doi: [10.3847/1538-4357/ad4a2a](https://doi.org/10.3847/1538-4357/ad4a2a)
- Jerkstrand, A., Fransson, C., Maguire, K., et al. 2012, *A&A*, 546, A28, doi: [10.1051/0004-6361/201219528](https://doi.org/10.1051/0004-6361/201219528)
- Jerkstrand, A., Smartt, S. J., Fraser, M., et al. 2014, *Monthly Notices of the Royal Astronomical Society*, 439, 3694, doi: [10.1093/mnras/stu221](https://doi.org/10.1093/mnras/stu221)
- Johnson, H. L., Mitchell, R. I., Iriarte, B., & Wisniewski, W. Z. 1966, *Communications of the Lunar and Planetary Laboratory*, 4, 99
- Koribalski, B. S., Staveley-Smith, L., Kilborn, V. A., et al. 2004, *The Astronomical Journal*, 128, 16, doi: [10.1086/421744](https://doi.org/10.1086/421744)
- Leonard, D. C., Filippenko, A. V., Li, W., et al. 2002, *The Astronomical Journal*, 124, 2490, doi: [10.1086/343771](https://doi.org/10.1086/343771)
- Li, G., Hu, M., Li, W., et al. 2024, *Nature*, 627, 754, doi: [10.1038/s41586-023-06843-6](https://doi.org/10.1038/s41586-023-06843-6)
- Li, L., Zhai, Q., Zhang, J., & Wang, X. 2023, *Transient Name Server Classification Report*, 2023-241, 1
- Lin, H., Zhang, J., Wang, X., et al. 2025, *Monthly Notices of the Royal Astronomical Society*, staf893, doi: [10.1093/mnras/staf893](https://doi.org/10.1093/mnras/staf893)
- Maguire, K., Di Carlo, E., Smartt, S. J., et al. 2010, *Monthly Notices of the Royal Astronomical Society*, 404, 981, doi: [10.1111/j.1365-2966.2010.16332.x](https://doi.org/10.1111/j.1365-2966.2010.16332.x)
- Maguire, K., Jerkstrand, A., Smartt, S. J., et al. 2012, *MNRAS*, 420, 3451, doi: [10.1111/j.1365-2966.2011.20276.x](https://doi.org/10.1111/j.1365-2966.2011.20276.x)
- Murai, Y., Tanaka, M., Kawabata, M., et al. 2024, *Monthly Notices of the Royal Astronomical Society*, 528, 4209, doi: [10.1093/mnras/stae170](https://doi.org/10.1093/mnras/stae170)
- Nicholl, M. 2018, *Research Notes of the American Astronomical Society*, 2, 230, doi: [10.3847/2515-5172/aaf799](https://doi.org/10.3847/2515-5172/aaf799)
- Pastorello, A., Sauer, D., Taubenberger, S., et al. 2006, *Monthly Notices of the Royal Astronomical Society*, 370, 1752, doi: [10.1111/j.1365-2966.2006.10587.x](https://doi.org/10.1111/j.1365-2966.2006.10587.x)
- Pearson, J., Hosseinzadeh, G., Sand, D. J., et al. 2023, *The Astrophysical Journal*, 945, 107, doi: [10.3847/1538-4357/acb8a9](https://doi.org/10.3847/1538-4357/acb8a9)
- Popov, D. V. 1993, *ApJ*, 414, 712, doi: [10.1086/173117](https://doi.org/10.1086/173117)
- Pun, C. S., Kirshner, R. P., Sonneborn, G., et al. 1995, *Astrophysical Journal Supplement v. 99*, p. 223, 99, 223
- Quimby, R. M., Wheeler, J. C., Höflich, P., et al. 2007, *The Astrophysical Journal*, 666, 1093, doi: [10.1086/520532](https://doi.org/10.1086/520532)
- Ravi, A. P., Valenti, S., Dong, Y., et al. 2025, *The Astrophysical Journal*, 982, 12, doi: [10.3847/1538-4357/adb0bb](https://doi.org/10.3847/1538-4357/adb0bb)
- Reguitti, A., Pastorello, A., Smartt, S. J., et al. 2025, *A&A*, 698, A129, doi: [10.1051/0004-6361/202554388](https://doi.org/10.1051/0004-6361/202554388)
- Rehemtulla, N., Jacobson-Galán, W. V., Singh, A., et al. 2025, *The Astrophysical Journal*, 985, 241, doi: [10.3847/1538-4357/adcf1e](https://doi.org/10.3847/1538-4357/adcf1e)
- Sand, D. J., Wyatt, S. D., Janzen, D., et al. 2023, *Transient Name Server Discovery Report*, 2023-223, 1
- Science Software Branch at STScI. 2012., *Astrophysics Source Code Library*, record ascl:1207.011 <http://ascl.net/1207.011>
- Shrestha, M., Bostroem, K. A., Sand, D. J., et al. 2024, *ApJL*, 972, L15, doi: [10.3847/2041-8213/ad6907](https://doi.org/10.3847/2041-8213/ad6907)
- Shrestha, M., Pearson, J., Wyatt, S., et al. 2024, *The Astrophysical Journal*, 961, 247, doi: [10.3847/1538-4357/ad11e1](https://doi.org/10.3847/1538-4357/ad11e1)
- Smith, N. 2014, *ARA&A*, 52, 487, doi: [10.1146/annurev-astro-081913-040025](https://doi.org/10.1146/annurev-astro-081913-040025)
- Smith, N., Pearson, J., Sand, D. J., et al. 2023, *ApJ*, 956, 46, doi: [10.3847/1538-4357/acf366](https://doi.org/10.3847/1538-4357/acf366)
- Soumagnac, M. T., Ganot, N., Irani, I., et al. 2020, *The Astrophysical Journal*, 902, 6, doi: [10.3847/1538-4357/abb247](https://doi.org/10.3847/1538-4357/abb247)
- Spiro, S., Pastorello, A., Pumo, M. L., et al. 2014, *MNRAS*, 439, 2873, doi: [10.1093/mnras/stu156](https://doi.org/10.1093/mnras/stu156)
- Stetson, P. B. 1987, *PASP*, 99, 191, doi: [10.1086/131977](https://doi.org/10.1086/131977)
- Szalai, T., Vinkó, J., Könyves-Tóth, R., et al. 2019, *The Astrophysical Journal*, 876, 19, doi: [10.3847/1538-4357/ab12d0](https://doi.org/10.3847/1538-4357/ab12d0)
- Tartaglia, L., Pastorello, A., Sollerman, J., et al. 2020, *A&A*, 635, A39, doi: [10.1051/0004-6361/201936553](https://doi.org/10.1051/0004-6361/201936553)
- Teja, R. S., Singh, A., Sahu, D. K., et al. 2022, *The Astrophysical Journal*, 930, 34, doi: [10.3847/1538-4357/ac610b](https://doi.org/10.3847/1538-4357/ac610b)
- Teja, R. S., Singh, A., Sahu, D. K., et al. 2023, *The Astrophysical Journal*, 954, 155, doi: [10.3847/1538-4357/acdf5e](https://doi.org/10.3847/1538-4357/acdf5e)
- Uomoto, A. 1986, *ApJL*, 310, L35, doi: [10.1086/184777](https://doi.org/10.1086/184777)
- Valerin, G., Pumo, M. L., Pastorello, A., et al. 2022, *MNRAS*, 513, 4983, doi: [10.1093/mnras/stac1182](https://doi.org/10.1093/mnras/stac1182)
- Van Dyk, S. D., de Graw, A., Baer-Way, R., et al. 2022, *Monthly Notices of the Royal Astronomical Society*, 519, 471, doi: [10.1093/mnras/stac3549](https://doi.org/10.1093/mnras/stac3549)
- Vasylyev, S. S., Filippenko, A. V., Vogl, C., et al. 2022, *The Astrophysical Journal*, 934, 134, doi: [10.3847/1538-4357/ac7220](https://doi.org/10.3847/1538-4357/ac7220)

- Wang, C.-J., Bai, J.-M., Fan, Y.-F., et al. 2019, *Research in Astronomy and Astrophysics*, 19, 149, doi: [10.1088/1674-4527/19/10/149](https://doi.org/10.1088/1674-4527/19/10/149)
- Weil, K. E., Fesen, R. A., Patnaude, D. J., & Milisavljevic, D. 2020, *The Astrophysical Journal*, 900, 11, doi: [10.3847/1538-4357/aba4b1](https://doi.org/10.3847/1538-4357/aba4b1)
- Xiang, D., Mo, J., Wang, X., et al. 2024, *ApJL*, 969, L15, doi: [10.3847/2041-8213/ad54b3](https://doi.org/10.3847/2041-8213/ad54b3)
- Yang, Y., Wen, X., Wang, L., et al. 2025, *Science Advances*, 11, 24.2925, doi: [10.1126/sciadv.adx2925](https://doi.org/10.1126/sciadv.adx2925)
- Yang, S., Sollerman, J., Strotjohann, N. L., et al. 2021, *A&A*, 655, A90, doi: [10.1051/0004-6361/202141244](https://doi.org/10.1051/0004-6361/202141244)
- Yaron, O., Perley, D. A., Gal-Yam, A., et al. 2017, *Nature Physics*, 13, 510, doi: [10.1038/nphys4025](https://doi.org/10.1038/nphys4025)
- Zhang, J., Wang, X., Mazzali, P. A., et al. 2014, *ApJ*, 797, 5, doi: [10.1088/0004-637X/797/1/5](https://doi.org/10.1088/0004-637X/797/1/5)
- Zhang, J., Wang, X., József, V., et al. 2020, *Monthly Notices of the Royal Astronomical Society*, 498, 84, doi: [10.1093/mnras/staa2273](https://doi.org/10.1093/mnras/staa2273)
- Zhang, J., Lin, H., Wang, X., et al. 2023, *Science Bulletin*, 68, 2548, doi: [10.1016/j.scib.2023.09.015](https://doi.org/10.1016/j.scib.2023.09.015)
- Zhang, J., Dessart, L., Wang, X., et al. 2024, *ApJL*, 970, L18, doi: [10.3847/2041-8213/ad5da4](https://doi.org/10.3847/2041-8213/ad5da4)
- Zhang, T., Wang, X., Wu, C., et al. 2012, *AJ*, 144, 131, doi: [10.1088/0004-6256/144/5/131](https://doi.org/10.1088/0004-6256/144/5/131)
- Zimmerman, E. A., Irani, I., Chen, P., et al. 2024, *Nature*, 627, 759, doi: [10.1038/s41586-024-07116-6](https://doi.org/10.1038/s41586-024-07116-6)

## APPENDIX

## A. PHOTOMETRIC AND SPECTROSCOPIC DATA

This section presents the observational data for SN 2023axu. The local photometric standard stars in the field of SN 2023axu are provided in Table A1. The photometric data from the LJT, WMS, REM, and Schmidt telescopes are provided in Table A2, ZTF and ATLAS photometric data are presented in Table A3, HST photometric data are presented in Table A4, while the log of spectroscopic observations obtained with the LJT, including epoch, exposure time, and configuration, is given in Table A5.

**Table A1.** Local photometric standard stars in the field of SN 2023axu

Star	B (mag)	V (mag)	g (mag)	r (mag)	i (mag)	z (mag)	H(mag)
1	16.177(0.09)	14.653(0.08)	15.30(0.01)	14.25(0.01)	13.79(0.01)	13.46(0.01)	11.611(0.03)
2	14.838(0.06)	14.192(0.09)	14.44(0.01)	13.98(0.01)	13.83(0.01)	13.75(0.01)	12.541(0.03)
3	18.983(0.09)	17.737(0.05)	16.97(0.01)	16.26(0.01)	15.97(0.01)	15.85(0.02)	15.284(0.14)
4	16.236(0.04)	14.859(0.13)	15.73(0.01)	14.30(0.01)	13.70(0.01)	13.28(0.01)	11.059(0.03)
5	15.798(0.02)	14.727(0.13)	15.34(0.01)	14.41(0.01)	14.05(0.01)	13.82(0.01)	12.137(0.02)
6	17.095(0.15)	16.183(0.13)	16.71(0.01)	16.01(0.01)	15.77(0.01)	15.68(0.02)	14.21(0.05)
7	14.44(0.02)	13.756(0.08)	13.18(0.01)	12.43(0.01)	12.10(0.01)	12.28(0.02)	12.123(0.02)
8	15.185(0.04)	14.522(0.07)	14.80(0.01)	14.28(0.01)	14.12(0.01)	14.04(0.01)	12.802(0.03)
9	14.618(0.03)	13.962(0.14)	14.23(0.01)	13.74(0.01)	14.12(0.02)	13.51(0.01)	12.363(0.02)

**Table A2.** Journal of photometric observations of SN 2023axu.

MJD	Epoch (day) <sup>a</sup>	B (mag)	V (mag)	g (mag)	r (mag)	i (mag)	z (mag)	H (mag)	Facility
59972.68	1.18	...	...	15.23(0.04)	15.25(0.02)	15.30(0.05)	...	...	LJT
59974.71	3.21	15.14(0.01)	14.82(0.01)	14.83(0.05)	14.67(0.04)	14.70(0.05)	...	...	LJT
59976.70	5.2	15.08(0.01)	14.71(0.01)	14.76(0.06)	14.53(0.04)	14.49(0.04)	...	...	LJT
59977.69	6.19	15.04(0.01)	14.67(0.01)	14.71(0.05)	14.48(0.11)	14.24(0.35)	...	...	LJT
59979.64	8.14	15.04(0.02)	14.66(0.01)	14.70(0.07)	14.41(0.05)	14.41(0.05)	...	...	LJT
59981.58	10.08	15.07(0.02)	14.68(0.01)	14.74(0.06)	14.45(0.06)	14.46(0.03)	...	...	LJT
59982.74	11.24	15.12(0.02)	14.70(0.01)	14.76(0.04)	14.41(0.04)	14.45(0.05)	...	...	LJT
59985.61	14.11	15.14(0.02)	14.72(0.01)	14.83(0.06)	14.45(0.06)	14.49(0.03)	...	...	LJT
59989.52	18.02	...	...	14.86(0.04)	14.41(0.05)	14.41(0.06)	...	...	LJT
59990.60	19.09	...	...	14.81(0.07)	14.49(0.06)	14.42(0.08)	...	...	WMS
59990.64	19.14	15.31(0.01)	14.74(0.01)	14.90(0.05)	14.44(0.06)	14.45(0.09)	...	...	LJT
59991.59	20.08	...	...	15.01(0.06)	14.41(0.09)	14.36(0.09)	...	...	WMS
59992.59	21.09	...	...	15.00(0.05)	14.45(0.06)	14.25(0.04)	...	...	WMS
59993.57	22.06	...	...	15.01(0.08)	14.43(0.05)	14.19(0.05)	...	...	WMS
59994.59	23.08	...	...	15.03(0.05)	14.43(0.04)	14.39(0.07)	...	...	WMS
59995.57	24.06	...	...	15.00(0.07)	14.40(0.09)	14.25(0.04)	...	...	WMS
59996.56	25.06	...	...	15.06(0.05)	14.42(0.06)	14.18(0.09)	...	...	WMS
59998.58	27.07	...	...	15.16(0.08)	14.41(0.06)	14.41(0.07)	...	...	WMS
60000.57	29.06	...	...	15.13(0.05)	14.45(0.05)	14.38(0.10)	...	...	WMS
60001.55	30.05	...	...	15.15(0.03)	14.49(0.08)	14.33(0.08)	...	...	WMS
60002.55	31.05	...	...	15.16(0.07)	14.48(0.06)	14.33(0.07)	...	...	WMS

Table A2 – Continued

MJD	Epoch (day) <sup>a</sup>	B (mag)	V (mag)	g (mag)	r (mag)	i (mag)	z (mag)	H (mag)	Facility
60003.56	32.06	...	...	15.20(0.08)	14.53(0.07)	14.40(0.07)	...	...	WMS
60004.53	33.03	15.72(0.01)	14.87(0.01)	15.15(0.06)	14.47(0.08)	14.45(0.05)	14.33(0.04)	...	LJT
60006.78	35.28	15.85(0.03)	14.90(0.02)	...	...	...	...	...	Schmidt
60010.53	39.03	15.82(0.01)	...	15.2(0.05)	14.48(0.07)	14.44(0.08)	...	...	LJT
60015.55	44.05	15.93(0.01)	14.94(0.01)	15.28(0.02)	14.52(0.03)	...	...	...	LJT
60027.54	56.04	16.12(0.01)	15.05(0.01)	15.43(0.06)	14.65(0.08)	14.54(0.02)	14.40(0.03)	...	LJT
60028.03	56.53	...	...	15.39(0.06)	14.22(0.05)	14.12(0.06)	14.43(0.07)	13.02 (0.06)	rem
60032.04	60.54	...	...	15.37(0.04)	14.63(0.03)	14.48(0.05)	14.41(0.07)	13.13 (0.06)	rem
60037.01	65.51	...	...	15.52(0.06)	14.63(0.04)	14.52(0.04)	14.41(0.08)	13.17 (0.08)	rem
60041.02	69.52	...	...	15.47(0.06)	14.70(0.03)	14.59(0.08)	14.52(0.08)	13.16 (0.08)	rem
60041.53	70.03	16.31(0.01)	15.18(0.01)	15.57(0.04)	14.69(0.08)	14.64(0.07)	14.43(0.05)	...	LJT
60045.02	73.52	...	...	15.54(0.05)	14.71(0.07)	14.64(0.06)	14.54(0.07)	13.19 (0.07)	rem
60046.53	75.03	16.35(0.01)	15.22(0.01)	...	14.72(0.05)	14.65(0.06)	14.52(0.07)	...	LJT
60049.02	77.52	...	...	15.52(0.06)	14.70(0.06)	14.66(0.08)	14.47(0.08)	13.20 (0.06)	rem
60049.53	78.03	16.23(0.09)	15.27(0.06)	...	14.76(0.10)	14.77(0.12)	14.44(0.08)	...	LJT
60052.53	81.03	16.46(0.02)	15.31(0.01)	15.78(0.03)	14.85(0.04)	14.78(0.03)	14.58(0.04)	...	LJT
60053.02	81.52	...	...	15.66(0.05)	14.92(0.11)	14.76(0.09)	14.60(0.07)	13.22 (0.07)	rem
60057.05	85.55	...	...	15.79(0.05)	14.89(0.03)	14.80(0.04)	14.62(0.06)	13.31 (0.08)	rem
60058.53	87.03	16.59(0.03)	15.44(0.01)	15.93(0.04)	14.95(0.05)	14.88(0.02)	14.68(0.04)	...	LJT
60061.04	89.54	...	...	15.82(0.08)	15.01(0.12)	14.90(0.08)	14.71(0.10)	13.39 (0.06)	rem
60065.05	93.55	...	...	15.97(0.13)	14.96(0.08)	14.71(0.07)	14.82(0.10)	13.51 (0.07)	rem
60069.05	97.55	...	...	16.66(0.19)	15.30(0.07)	15.28(0.10)	15.18(0.12)	13.69 (0.07)	rem
60073.05	101.55	...	...	17.20(0.22)	15.55(0.05)	15.48(0.09)	15.32(0.11)	13.83 (0.06)	rem
60077.06	105.56	...	...	17.14(0.15)	15.95(0.14)	16.06(0.21)	15.56(0.11)	13.93 (0.08)	rem
60239.89	268.39	...	18.66(0.03)	19.09(0.09)	17.53(0.07)	17.90(0.08)	...	...	LJT
60255.82	284.32	...	...	...	17.73(0.06)	17.95(0.42)	...	...	LJT
60270.82	299.32	...	18.96(0.05)	19.26(0.11)	17.91(0.05)	18.24(0.07)	17.78(0.08)	...	LJT
60368.51	397.01	...	...	...	19.49(0.16)	19.41(0.15)	19.12(0.15)	...	LJT
60370.56	399.06	...	...	...	19.36(0.11)	19.17(0.13)	...	...	LJT
60382.54	411.04	...	...	...	19.26(0.34)	19.12(0.17)	...	...	LJT

Table A3. ATLAS and ZTF observations of SN 2023axu.

MJD	Epoch (day)	MAG(err)	filter	TELESCOPE
59971.91	0.41	15.93(0.01)	c	ATLAS
59972.27	0.77	15.47(0.03)	r	ZTF
59973.13	1.63	14.95(0.01)	o	ATLAS
59974.54	3.04	14.59(0.01)	o	ATLAS
59975.87	4.37	14.51(0.01)	o	ATLAS
59977.15	5.65	14.42(0.01)	o	ATLAS
59978.51	7.01	14.39(0.01)	o	ATLAS
59979.21	7.71	14.40(0.03)	r	ZTF
59979.92	8.42	14.39(0.01)	o	ATLAS
59981.15	9.65	14.38(0.01)	o	ATLAS
59982.17	10.67	14.32(0.01)	o	ATLAS
59982.23	10.73	14.38(0.02)	r	ZTF

Table A3 – Continued

MJD	Epoch (day)	MAG(err)	filter	TELESCOPE
59983.54	12.04	14.36(0.01)	o	ATLAS
59984.90	13.40	14.41(0.01)	o	ATLAS
59985.21	13.71	14.38(0.02)	r	ZTF
59985.88	14.38	14.40(0.01)	o	ATLAS
59987.15	15.65	14.40(0.01)	o	ATLAS
59988.89	17.39	14.37(0.01)	o	ATLAS
59989.89	18.39	14.36(0.01)	o	ATLAS
59991.14	19.64	14.70(0.01)	c	ATLAS
59991.19	19.69	14.84(0.02)	g	ZTF
59991.21	19.71	14.31(0.02)	r	ZTF
59993.84	22.34	14.36(0.01)	o	ATLAS
59995.08	23.58	14.75(0.01)	c	ATLAS
59997.89	26.39	14.35(0.01)	o	ATLAS
60003.07	31.57	14.40(0.01)	o	ATLAS
60005.86	34.36	14.40(0.01)	o	ATLAS
60007.11	35.61	14.41(0.01)	o	ATLAS
60011.48	39.98	14.44(0.01)	o	ATLAS
60013.23	41.73	14.42(0.02)	r	ZTF
60013.25	41.75	15.24(0.03)	g	ZTF
60013.89	42.39	14.47(0.01)	o	ATLAS
60015.14	43.64	14.45(0.01)	o	ATLAS
60017.18	45.68	15.19(0.05)	g	ZTF
60017.81	46.31	14.99(0.16)	c	ATLAS
60019.06	47.56	14.45(0.01)	o	ATLAS
60021.15	49.65	14.49(0.02)	r	ZTF
60021.84	50.34	15.03(0.01)	c	ATLAS
60023.08	51.58	14.46(0.01)	o	ATLAS
60025.78	54.28	15.07(0.02)	c	ATLAS
60027.05	55.55	14.53(0.01)	o	ATLAS
60029.83	58.33	15.10(0.01)	c	ATLAS
60030.15	58.65	15.44(0.03)	g	ZTF
60031.11	59.61	14.55(0.01)	o	ATLAS
60033.77	62.27	14.55(0.01)	o	ATLAS
60035.82	64.32	14.56(0.01)	o	ATLAS
60036.15	64.65	15.54(0.03)	g	ZTF
60036.17	64.67	14.58(0.03)	r	ZTF
60037.03	65.53	14.56(0.01)	o	ATLAS
60038.83	67.33	14.58(0.01)	o	ATLAS
60040.08	68.58	14.62(0.01)	o	ATLAS
60041.82	70.32	14.62(0.01)	o	ATLAS
60043.08	71.58	14.63(0.01)	o	ATLAS
60044.37	72.87	14.68(0.01)	o	ATLAS
60046.05	74.55	15.29(0.01)	c	ATLAS
60047.78	76.28	14.71(0.02)	o	ATLAS
60049.07	77.57	15.35(0.01)	c	ATLAS
60050.81	79.31	14.72(0.01)	o	ATLAS

Table A3 – Continued

MJD	Epoch (day)	MAG(err)	filter	TELESCOPE
60052.08	80.58	15.40(0.01)	c	ATLAS
60053.80	82.30	14.79(0.01)	o	ATLAS
60056.06	84.56	15.49(0.01)	c	ATLAS
60058.06	86.56	15.54(0.01)	c	ATLAS
60062.36	90.86	14.98(0.09)	o	ATLAS
60065.81	94.31	15.09(0.02)	o	ATLAS
60067.04	95.54	15.15(0.01)	o	ATLAS
60068.38	96.88	15.23(0.02)	o	ATLAS
60070.74	99.24	15.34(0.01)	o	ATLAS
60072.02	100.52	15.37(0.02)	o	ATLAS
60074.03	102.53	15.56(0.01)	o	ATLAS
60074.74	103.24	16.47(0.02)	c	ATLAS
60080.74	109.24	16.88(0.03)	c	ATLAS
60083.76	112.26	17.00(0.03)	c	ATLAS
60084.98	113.48	16.18(0.02)	o	ATLAS
60085.00	113.50	16.14(0.02)	o	ATLAS
60092.73	121.23	16.21(0.03)	o	ATLAS
60180.14	208.64	16.98(0.05)	o	ATLAS
60183.15	211.65	17.00(0.03)	o	ATLAS
60187.34	215.84	17.06(0.06)	o	ATLAS
60189.13	217.63	17.08(0.06)	o	ATLAS
60204.39	232.89	17.16(0.03)	o	ATLAS
60210.11	238.61	18.26(0.06)	c	ATLAS
60211.34	239.84	17.30(0.04)	o	ATLAS
60214.34	242.84	17.38(0.05)	o	ATLAS
60215.48	243.98	18.82(0.16)	g	ZTF
60216.01	244.51	17.20(0.10)	o	ATLAS
60217.34	245.84	17.22(0.06)	o	ATLAS
60219.09	247.59	17.40(0.06)	o	ATLAS
60221.12	249.62	17.48(0.07)	o	ATLAS
60222.38	250.88	17.34(0.05)	o	ATLAS
60222.46	250.96	18.85(0.16)	g	ZTF
60222.50	251.00	17.29(0.03)	r	ZTF
60224.46	252.96	18.91(0.13)	g	ZTF
60224.50	253.00	17.35(0.04)	r	ZTF
60227.97	256.47	17.49(0.06)	o	ATLAS
60228.02	256.52	17.56(0.04)	o	ATLAS
60228.43	256.93	18.84(0.14)	g	ZTF
60229.31	257.81	17.48(0.04)	o	ATLAS
60231.45	259.95	18.96(0.13)	g	ZTF
60231.50	260.00	17.45(0.04)	r	ZTF
60234.06	262.56	17.54(0.04)	o	ATLAS
60235.49	263.99	18.90(0.12)	g	ZTF
60237.46	265.96	18.95(0.12)	g	ZTF
60237.50	266.00	17.48(0.04)	r	ZTF
60239.44	267.94	17.51(0.04)	r	ZTF

Table A3 – Continued

MJD	Epoch (day)	MAG(err)	filter	TELESCOPE
60239.48	267.98	19.00(0.10)	g	ZTF
60240.30	268.80	17.65(0.05)	o	ATLAS
60241.29	269.79	17.65(0.08)	o	ATLAS
60242.04	270.54	17.69(0.06)	o	ATLAS
60243.09	271.59	17.59(0.07)	o	ATLAS
60244.30	272.80	17.42(0.13)	o	ATLAS
60244.40	272.90	19.10(0.26)	g	ZTF
60246.50	275.00	17.64(0.05)	r	ZTF
60248.00	276.50	17.81(0.11)	o	ATLAS
60248.01	276.51	17.79(0.11)	o	ATLAS
60249.05	277.55	17.76(0.09)	o	ATLAS
60249.39	277.89	19.07(0.23)	g	ZTF
60249.47	277.97	17.76(0.14)	r	ZTF
60251.36	279.86	18.94(0.17)	g	ZTF
60251.43	279.93	17.67(0.06)	r	ZTF
60253.30	281.80	17.59(0.05)	o	ATLAS
60253.38	281.88	17.69(0.05)	r	ZTF
60253.45	281.95	19.22(0.16)	g	ZTF
60254.46	282.96	19.10(0.13)	g	ZTF
60254.50	283.00	17.73(0.05)	r	ZTF
60255.28	283.78	17.77(0.05)	o	ATLAS
60256.27	284.77	17.84(0.05)	o	ATLAS
60258.38	286.88	19.12(0.19)	g	ZTF
60258.44	286.94	17.77(0.04)	r	ZTF
60259.99	288.49	18.81(0.10)	c	ATLAS
60260.05	288.55	18.82(0.09)	c	ATLAS
60260.35	288.85	19.26(0.07)	g	ZTF
60260.37	288.87	17.78(0.05)	r	ZTF
60262.27	290.77	17.73(0.05)	o	ATLAS
60262.47	290.97	17.83(0.05)	r	ZTF
60262.54	291.04	19.17(0.13)	g	ZTF
60264.28	292.78	17.94(0.06)	o	ATLAS
60266.07	294.57	18.91(0.10)	c	ATLAS
60268.25	296.75	17.95(0.06)	o	ATLAS
60270.23	298.73	18.08(0.08)	o	ATLAS
60279.00	307.50	18.11(0.09)	o	ATLAS
60279.00	307.50	18.08(0.09)	o	ATLAS
60280.99	309.49	18.06(0.07)	o	ATLAS
60282.34	310.84	18.10(0.04)	o	ATLAS
60286.93	315.43	18.22(0.08)	o	ATLAS
60287.29	315.79	19.53(0.25)	g	ZTF
60288.40	316.90	18.20(0.08)	r	ZTF
60288.40	316.90	18.22(0.03)	r	ZTF
60288.44	316.94	19.46(0.16)	g	ZTF
60288.44	316.94	19.59(0.12)	g	ZTF
60289.30	317.80	18.22(0.03)	o	ATLAS

Table A3 – Continued

MJD	Epoch (day)	MAG(err)	filter	TELESCOPE
60289.34	317.84	18.14(0.07)	r	ZTF
60290.24	318.74	18.23(0.04)	o	ATLAS
60290.37	318.87	19.48(0.16)	g	ZTF
60290.37	318.87	19.46(0.09)	g	ZTF
60290.38	318.88	18.15(0.04)	r	ZTF
60290.38	318.88	18.13(0.02)	r	ZTF
60291.02	319.52	18.25(0.07)	o	ATLAS
60291.35	319.85	18.17(0.06)	r	ZTF
60292.02	320.52	18.29(0.07)	o	ATLAS
60293.31	321.81	18.02(0.07)	o	ATLAS
60294.71	323.21	18.23(0.07)	o	ATLAS
60295.96	324.46	18.24(0.07)	o	ATLAS
60297.21	325.71	18.29(0.10)	o	ATLAS
60298.22	326.72	18.29(0.08)	o	ATLAS
60299.03	327.53	18.40(0.08)	o	ATLAS
60306.36	334.86	18.38(0.14)	r	ZTF
60308.38	336.88	18.33(0.26)	r	ZTF
60314.28	342.78	19.64(0.23)	g	ZTF
60314.28	342.78	19.68(0.12)	g	ZTF
60314.42	342.92	18.45(0.09)	r	ZTF
60314.42	342.92	18.47(0.05)	r	ZTF
60322.25	350.75	18.73(0.14)	r	ZTF
60322.27	350.77	19.92(0.25)	g	ZTF
60324.22	352.72	19.62(0.22)	g	ZTF
60324.24	352.74	18.72(0.09)	r	ZTF
60324.24	352.74	18.74(0.06)	r	ZTF
60326.23	354.73	18.68(0.07)	r	ZTF
60326.32	354.82	19.76(0.22)	g	ZTF
60326.32	354.82	19.76(0.10)	g	ZTF
60334.21	362.71	18.89(0.25)	r	ZTF
60339.23	367.73	18.85(0.11)	r	ZTF
60339.23	367.73	18.89(0.07)	r	ZTF
60339.36	367.86	20.20(0.30)	g	ZTF
60352.24	380.74	19.06(0.11)	r	ZTF
60368.29	396.79	19.35(0.22)	r	ZTF
60368.29	396.79	19.42(0.19)	r	ZTF
60388.15	416.65	21.06(0.66)	g	ZTF
60390.15	418.65	19.58(0.20)	r	ZTF

**Table A4.** Photometric observations of SN 2023axu by HST

MJD	Epoch (day) <sup>a</sup>	F814W(mag)	F555W(mag)	F438W(mag)	F336W(mag)	F275W(mag)
60942.8	971.3	25.26(0.12)	26.27(0.15)	26.55(0.50)	>25.58	>24.58

<sup>a</sup>All of the data presented in this article were obtained from the MAST at the Space Telescope Science Institute. The specific observations analyzed can be accessed via [doi:10.17909/6djx-c648](https://doi.org/10.17909/6djx-c648).

**Table A5.** Journal of spectroscopic observations of SN 2023axu by LJT with YFOSC

Date (UT)	MJD	Epoch (day) <sup>a</sup>	Range (Å)	Disp. (Å pix <sup>-1</sup> )	Exp (s)	airmass
2023-01-28	59972.67	1.17	3600-8950	2.85	900	1.43
2023-01-30	59974.70	3.20	3600-8950	2.85	700	1.53
2023-02-01	59976.68	5.18	3600-8950	2.85	900	1.50
2023-02-04	59979.63	8.13	3600-8950	2.85	700	1.41
2023-02-06	59981.56	10.06	3600-8950	2.85	700	1.53
2023-02-07	59982.73	11.23	3600-8950	2.85	700	1.93
2023-02-12	59987.52	16.02	3600-8950	2.85	1200	1.69
2023-02-15	59990.62	19.12	3600-8950	2.85	1000	1.43
2023-02-24	59999.58	28.08	3600-8950	2.85	800	1.41
2023-03-01	60004.52	33.02	3600-8950	2.85	1000	1.47
2023-03-07	60010.53	39.03	3600-8950	2.85	1000	1.41
2023-03-12	60015.53	44.03	3600-8950	2.85	1000	1.41
2023-03-29	60032.53	61.03	3600-8950	2.85	1000	1.49
2023-04-06	60040.53	69.03	3600-8950	2.85	1000	1.62
2023-04-12	60046.54	75.04	3600-8950	2.85	1000	1.81
2023-11-11	60259.83	288.33	3600-8950	2.85	2800	1.44

<sup>a</sup>The epoch is relative to the explosion date, MJD = 59971.5.